

## **Tailoring the Morphology of Cellulose Nanocrystals via Controlled Aggregation**

*Kévin Ballu, Jia-Hui Lim, Thomas G. Parton, Richard M. Parker, Bruno Frka-Petesic, Alexei A. Lapkin, Yu Ogawa\*, Silvia Vignolini\**

Kévin Ballu, Dr Richard M Parker, Dr Bruno Frka-Petesic, Prof Silvia Vignolini

Yusuf Hamied Department of Chemistry, University of Cambridge, Cambridge CB2 1EW, United Kingdom

Jia-Hui Lim, Dr Yu Ogawa

University of Grenoble Alpes, CNRS, CERMAV, 38000 Grenoble, France

\* E-mail: [yu.ogawa@cermav.cnrs.fr](mailto:yu.ogawa@cermav.cnrs.fr)

Dr Thomas G Parton, Prof Silvia Vignolini

Department of Sustainable and Bio-inspired Materials, Max Planck Institute of Colloids and Interfaces, 14476 Potsdam, Germany

\* E-mail: [sv@mpikg.mpg.de](mailto:sv@mpikg.mpg.de)

Dr Bruno Frka-Petesic

International Institute for Sustainability with Knotted Chiral Meta Matter (WPI-SKCM<sup>2</sup>), Hiroshima University, Hiroshima 739-8526, Japan

Prof Alexei Lapkin

Department of Chemical Engineering and Biotechnology, University of Cambridge, Cambridge CB3 0AS, United Kingdom

Prof Alexei Lapkin

Innovative Center in Digital Molecular Technologies, Yusuf Hamied Department of Chemistry, University of Cambridge, Cambridge CB2 1EW, United Kingdom

**Keywords:** Cellulose Nanocrystals, Particle Morphology, Scanning Nanobeam Electron Diffraction, Cholesteric Liquid Crystals

**Abstract:**

Cellulose nanocrystals (CNCs) are bioderived nanoparticles that can be isolated from various sources of natural cellulose via acid hydrolysis. However, the link between particle morphological characteristics and their ensemble behavior is poorly understood, partly because of the difficulties in controlling the CNC morphology during their extraction process. In this work, the impacts of common post-hydrolysis treatments on the CNC morphology are investigated. The results indicate that the centrifugation step commonly applied during CNC purification favors the formation of composite particles made of aligned crystallites, referred to as “bundles”. Scanning nanobeam electron diffraction reveals that such bundles are associated preferentially along their hydrophobic faces. This is in stark contrast to the formation of misaligned composite particles that can be achieved with ionic treatments, where an uncontrolled aggregation occurs. The functional relevance of these morphological differences is demonstrated by their effect on the cholesteric self-organization of CNCs, with bundles found to exhibit a greater chiral enhancement, whereas the misaligned composite particles found to promote gelation. This study reveals the importance of the often-disregarded purification steps on the final morphology of CNCs and their resulting ensemble properties, thereby unlocking new routes for tailoring this promising material towards a variety of applications.

## 1. Introduction

Cellulose nanocrystals (CNCs) are colloiddally stable and elongated crystalline nanoparticles derived from native cellulose.<sup>[1,2]</sup> This nanomaterial has recently attracted significant interest for its sustainable sourcing and numerous potential applications, ranging from rheological modifiers and emulsion stabilizers to colorants and sensors.<sup>[3]</sup> However, further development of CNCs for these applications is broadly hindered by the difficulty in producing standardized CNCs.

The hydrolysis of wood cellulose with concentrated sulfuric acid, followed by various purification steps, is the most industrially relevant method of CNC extraction.<sup>[4]</sup> At the laboratory scale, purification usually consists of several rounds of centrifugation-redispersion in deionized water, which allows for the separation of the acidic supernatant from the pelletized CNCs, followed by dialysis against deionized water. The obtained colloidal suspension is electrostatically stabilized by the negatively charged sulfate half-ester groups ( $-\text{OSO}_3^-$ ) grafted onto their surface during hydrolysis.<sup>[5]</sup> Most previous studies investigating this approach focused on the hydrolysis parameters and their impact on the yield, while generally disregarding the impact of the subsequent purification steps as well as the resulting characteristics of the CNCs.<sup>[2]</sup> Consequently, organizations adopt different extraction protocols, resulting in CNCs with differing morphology and surface properties,<sup>[6,7]</sup> which leads to unpredictability in their amphiphilicity and self-organization.

The extraction of CNCs often leads to suspensions of morphologically diverse particles, containing both individual crystallites as well as composite particles made of multiple laterally aligned crystallites.<sup>[8-10]</sup> These composite particles, often referred to as “bundle-like” or “raft-like”, are of primary importance for various applications. For example, when CNCs undergo self-organization into a cholesteric liquid crystal, the proportion of the bundle-like subpopulation can be correlated with a decrease in the cholesteric pitch and a narrowing of the concentration range of the biphasic regime.<sup>[10]</sup> Moreover, composite particles are also involved in emulsion stabilization,<sup>[11]</sup> due to their influence on the wetting behavior of the CNCs.<sup>[12]</sup> On this basis, it has been proposed that the crystallites that make up the composite particles were preferentially associated along their hydrophobic faces.<sup>[12]</sup> However, whether these laterally associated composite particles predate the hydrolysis, and therefore might be related to the source,<sup>[8]</sup> or are synthetically formed during the process remains an open question.

In this work, we investigate the impact of the post-hydrolysis centrifugation step on the morphology of CNCs and we then compare it with the aggregation induced by divalent cations. Using transmission electron microscopy (TEM) and viscometry, we show that CNC purification by centrifugation favors the formation of laterally aligned composite particles, or “bundles”. We further confirm by scanning nanobeam electron diffraction (SNBED) that these bundles are preferentially associated through their hydrophobic faces. Conversely, aggregation with calcium chloride ( $\text{CaCl}_2$ ) leads to an irreversible increase in the average CNC size due to the formation of randomly associated composite particles that exhibit weaker internal cohesion. Comparative pitch measurements on the cholesteric phase show that the presence of bundles reduces the pitch (indicating enhanced chiral strength), while random aggregates made using  $\text{CaCl}_2$  instead promote gelation at a lower concentration.

## 2. Results and Discussion

### 2.1 Aggregation by Centrifugation

To explore the influence of post-hydrolysis centrifugation on CNC morphology, cotton derived cellulose was hydrolyzed into CNCs according to the conditions summarized in **Figure 1** and detailed in the Experimental Section. After quenching the hydrolysis reaction, part of the reaction mixture was isolated and never centrifuged (**C0**), while the remaining mixture was subjected to multiple rounds of centrifugation and re-dispersal of the pellet in ultrapure water. Aliquots of the mixture were isolated after one, two or three rounds of centrifugation, resulting in samples **C1**, **C2** and **C3** respectively. For storage purposes, **C0** and **C3** were charge neutralized with sodium hydroxide followed by concentration (< 15 wt%) to yield **C0-Na** and **C3-Na** respectively, without impacting their morphology, as indicated by DLS measurements (**Table S1**).

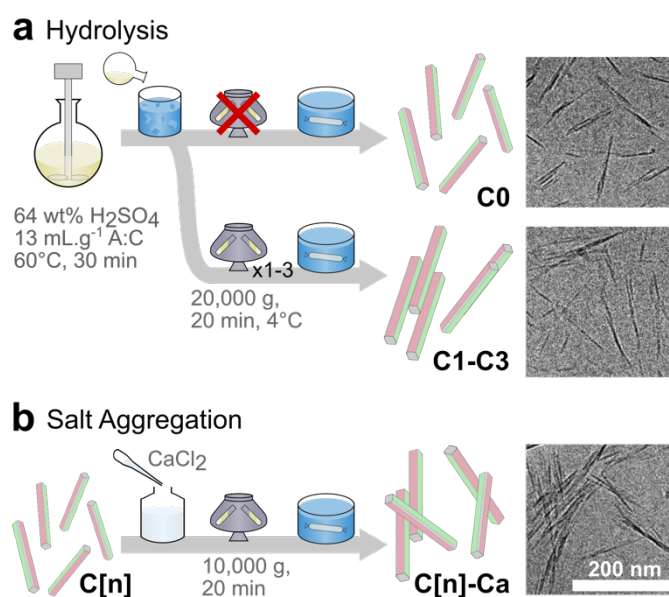


**Figure 1.** Scheme summarizing the preparation and resulting cryo-TEM images of **(a)** never centrifuged (**C0**) and centrifuged (**C1-C3**) CNCs, and **(b)** salt aggregated CNCs subsequently produced by calcium chloride addition followed by centrifugation (**C0-Ca** and **C3-Ca**). Example cryo-TEM images highlight the morphological differences of the CNCs produced by these protocols.

## 2.2 Morphological Analysis by TEM

The morphology of the different CNC samples was investigated by TEM, as exemplified in **Figure 2a**. Visual inspection of the TEM images revealed that each sample contained a variety of particle types, with both composite particles constituted of aligned subunits (referred to as bundles) as well as irregular composite particles, as commonly reported for wood and cotton-derived CNCs.<sup>[8,10]</sup> To draw meaningful conclusions on the differences in morphology between the never-centrifuged (**C0**) and centrifuged (**C1-C3**) CNCs, their morphological properties were quantified by manually tracing the contours of a large number of particles for each sample ( $N > 225$ ), as exemplified in **Figure 2b**. It is noteworthy that the presence of composite particles leads to inconsistencies in the literature regarding what is considered an individual CNC during particle analysis.<sup>[2]</sup> In this context, each discrete object on the TEM grid was considered a single CNC, regardless of whether it appeared as a single crystallite or as a composite object formed by multiple overlapping crystallites.

The morphological parameters extracted from the TEM image analysis are reported in **Figure 2c-f**. The values of the CNC bounding box length ( $L_b$ ) and width ( $W_b$ ) almost followed a log-normal distribution for all samples (see **Figure S5** and **Table S3**),<sup>[8,13]</sup> therefore pairwise statistical comparison between them was performed using a Mann–Whitney test on  $\ln(L_b)$  and  $\ln(W_b)$  (see **Table S4** and **Table S5** respectively). The dimensions of **C1-C3** were statistically similar but were significantly longer and consistently wider than for **C0** (although the latter difference was not statistically significant). These results were consistent with dynamic light scattering (DLS) measurements that showed a greater Z-averaged apparent hydrodynamic diameter (denoted  $Z$ ) for suspensions of **C1-C3** when compared to **C0** (**Figure 3a**).

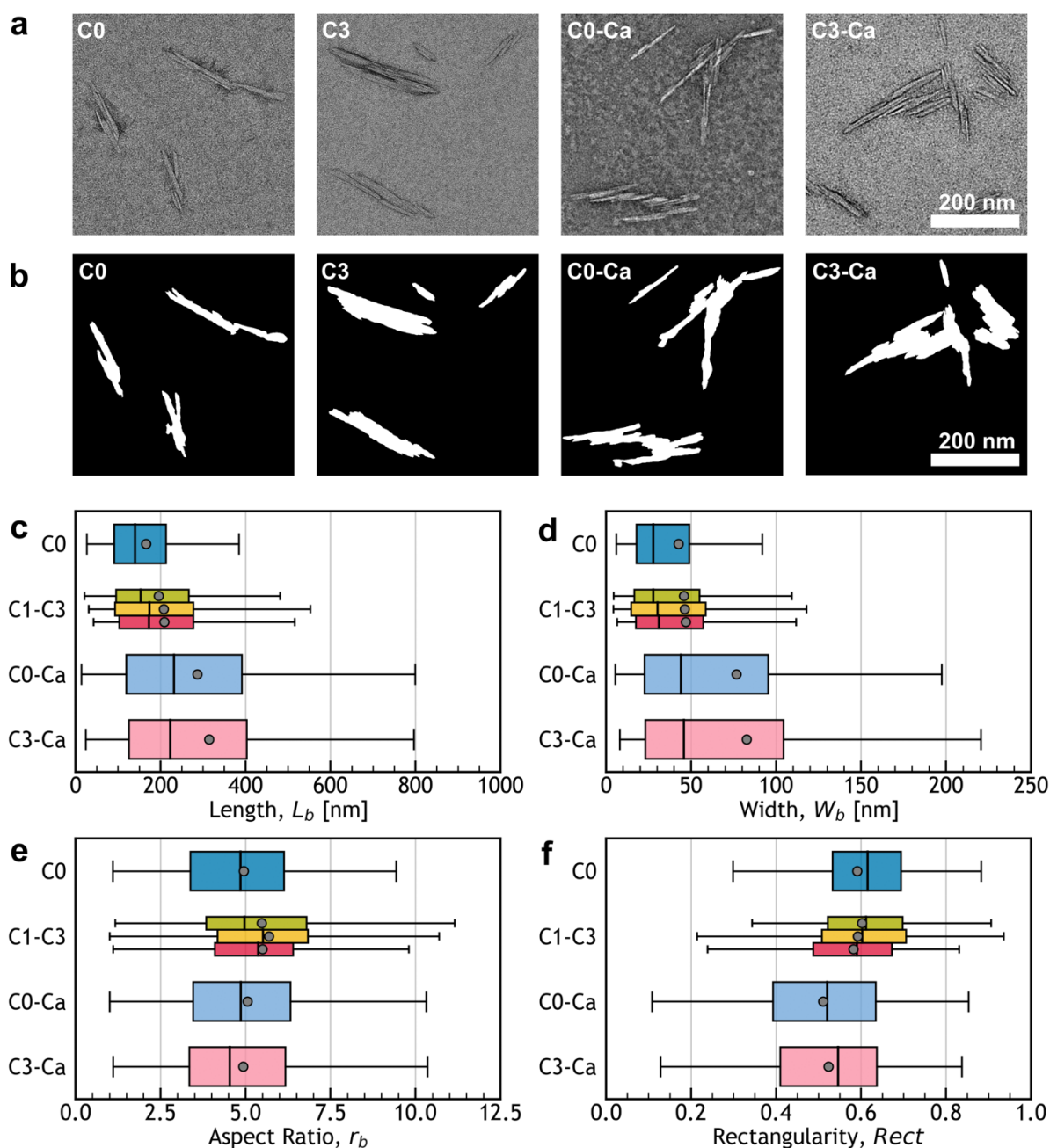


**Figure 2.** Analysis of the CNC morphology from TEM images. **(a)** Typical objects observed by TEM and **(b)** examples of the corresponding contoured shapes used for dimension extraction. **(c-f)** Boxplots of the morphological parameters extracted: (b) bounding box lengths ( $L_b$ ), (c) bounding box widths ( $W_b$ ),

(d) bounding box aspect ratios ( $r_b$ ), and (e) rectangularity ( $Rect$ ). Outliers are not displayed, full data is presented in **Figure S5** and **Figure S6** (Supporting Information); grey-filled circles indicate the average values.

The morphology of the particles was further examined by estimating their bounding box aspect ratio ( $r_b$ ) and rectangularity ( $Rect$ ) defined respectively as:

$$r_b = \frac{L_b}{W_b} \quad (1)$$

and

$$Rect = \frac{A}{L_b W_b} \quad (2)$$

where  $A$  is the projected particle area onto the TEM grid.<sup>[10]</sup> As presented in **Figure 2e** and in **Figure 2f** respectively,  $r_b$  and  $Rect$  followed skewed normal distributions for all samples (see also **Figure S6** and **Table S3**). Overall, **C0** exhibits slightly lower aspect ratios than **C1-C3**, but all had a similar rectangularity (see pairwise comparison in **Table S6** and **Table S7**). These results indicate that centrifugation during purification led to the formation of composite particles while retaining a similar shape. More specifically, for rod-like particles, this scaling infers the formation of composite particles constituted of aligned subunits (i.e. bundles).

As the morphological parameters for **C1-C3** in **Figure 2c-f** are almost identical, we deduce that only the first cycle of centrifugation (**C0** to **C1**) caused a significant increase in particle dimensions ( $L_b$ ,  $W_b$  and  $Z$ ). This finding may indicate that the degree of aggregation of the composite particles is intrinsically limited. An alternative explanation is related to the decrease in ionic strength after each successive redispersion of the CNC pellet in deionized water after centrifugation: it is possible that beyond **C1**, the stronger electrostatic repulsion between CNCs prevents the close contact necessary for aggregation.

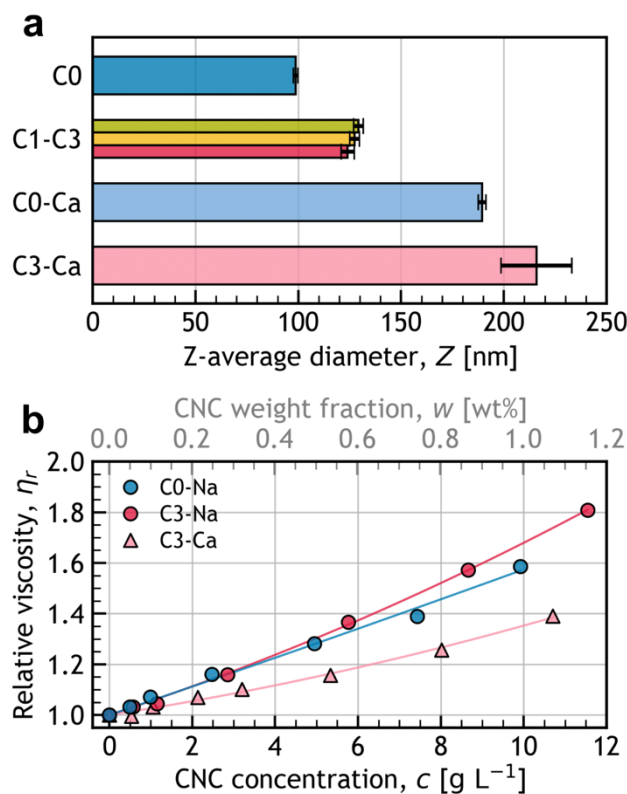


**Figure 3. (a)** DLS Z-average diameter ( $Z$ ) and **(b)** evolution of the relative viscosity ( $\eta_r$ ) as a function of the CNC concentration ( $c$ ) with best fit using Equation 3.

### 2.3 Aggregation by Salt Addition

To investigate this effect and better understand the impact of post-hydrolysis purification on CNC morphology, neutralized CNC suspensions (C0-Na and C3-Na) were centrifuged under controlled salt conditions. The protocol used can be broken down into four consequent steps: (i) suspension preparation with CaCl<sub>2</sub> at known ionic strength ( $I_{agg}$ ) and CNC weight fraction ( $w_{agg}$ ), (ii) aggregation, (iii) homogenization by mixing, (iv) dilution to 0.1 wt% CNC and an ionic strength as close as possible to 1 mM. The impact of aggregation time, centrifugation during aggregation and  $w_{agg}$  on the CNC Z-average diameter after dilution was investigated in a series of experiments presented in the Supporting Information (see Table S2, Figure S2 and Figure S3). These experiments were used to refine the aggregation protocol summarized in Figure 4a, that is with a fixed CNC weight fraction ( $w_{agg} = 6.5$  wt%) and a centrifugation step (20 min, 10,000 g) during the aggregation. Note that waiting for an hour or more before homogenization and dilution had no noticeable difference on the final particle size compared to using this centrifugation step (Table S2).

Using this approach, the evolution of the Z-average diameter of the CNCs as a function of salt type (NaCl vs CaCl<sub>2</sub>) and ionic strength ( $0 \leq I_{agg} \leq 80$  mM) were investigated. The resulting DLS intensity plots as a function of salt are presented in Figure S4 and the extracted Z-average diameters are plotted in Figure 4b. At  $I_{agg} = 0$  (i.e. without any added salt), centrifugation did not modify the size of any of the samples (see Figure 4b vs Figure 3a). This further supports our hypothesis that the size increase observed between C0 and C1 was enabled by the high ionic strength of the medium at that point in the purification process ( $I \approx 4050$  mM). In contrast,

increasing the salt concentration led to a sigmoidal growth of the Z-average diameter of the particles, with calcium leading to a much greater increase than for sodium (**Figure 4b**). These results suggest that the particle size increase caused by salt-induced aggregation followed by dilution is limited. Moreover, divalent ions are more potent than monovalent ions for inducing irreversible aggregation of CNCs, as previously reported for different polycations.<sup>[5,14–17]</sup> This can be explained by the irreversible formation of calcium bridges between CNCs, in addition to any shielding of the electrostatic interactions. Expanding upon these results, **C0-Na** and **C3-Na** were centrifuged in the presence of calcium chloride ( $I_{agg} = 40$  mM) followed by dialysis against water, to respectively produce **C0-Ca** and **C3-Ca**, collectively referred to as Ca-CNCs.

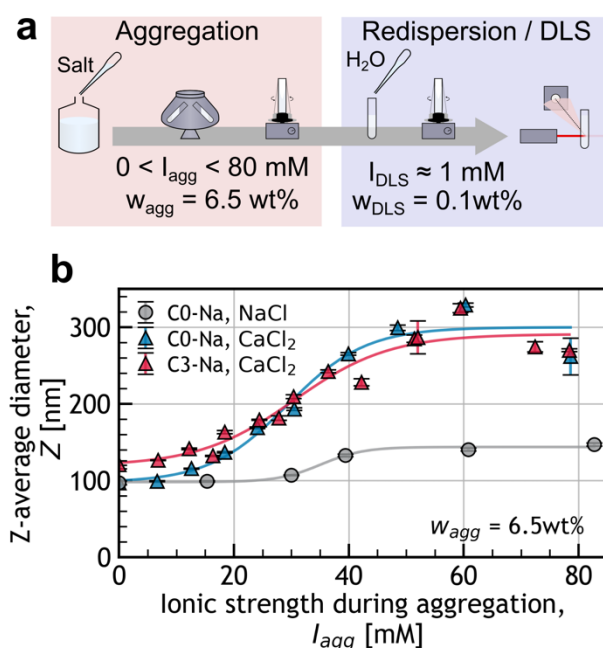


**Figure 4.** (a) Scheme summarizing the calcium aggregation process and (b) the impact of salt type (NaCl vs CaCl<sub>2</sub>) and ionic strength ( $I_{agg}$ ) at fixed weight fraction ( $w_{agg} = 6.5$  wt%) during aggregation on the resulting Z-average size ( $Z$ ), as measured after dilution to 0.1 wt% in an ionic strength as close as possible to 1 mM. The lines of best fit are presented as visual guides and were obtained from a logistic function.

Visual inspection of TEM images for **C0-Ca** and **C3-Ca** suggests that these samples contain a higher number of larger irregular composite particles compared to **C0** and **C3**. The extracted TEM size parameters  $L_b$  and  $W_b$ , as well as the DLS Z-averaged diameter ( $Z$ ), of the Ca-CNCs were larger than for other samples, irrespective of the initial CNC used to prepare them (**Figure 2c** and **Figure 2d** and pairwise comparison in **Table S4** and **Table S5**). This shows that exposure to calcium chloride results in particle association that is retained after extensive dialysis. The Ca-CNCs also generally exhibited a lower aspect ratio and rectangularity than the centrifuged CNCs, indicating that they are composed of misaligned components (**Figure 2e** and **Figure 2f** and pairwise comparison in **Table S6** and **Table S7**). Combining these results, we can infer that aggregation with calcium chloride leads to the irreversible association of crystallites into irregular particles. This conclusion is consistent with extended DLVO predictions for charged elongated rods, for which crossed association offers a lower energetic barrier to overcome compared to parallel association.<sup>[18,19]</sup> Upon rapid aggregation, this favors

the association of particles with a crossed geometry, despite the parallel association being more stable. Furthermore, this crossed-association mechanism is favored at high ionic strength<sup>[20]</sup> and was experimentally observed for charged CNCs.<sup>[14,21,22]</sup>

The comparison between **C0-Ca** and **C3-Ca** by TEM or by DLS leads to different trends (**Figure 2c-d** and **Figure 3a**). While all the morphological parameters extracted by TEM were similar for **C0-Ca** and **C3-Ca**, their Z-average diameters indicate that **C3-Ca** CNCs were larger. This discrepancy could be attributed to the higher polydispersity of these randomly-aggregated samples. Indeed, although DLS is an ensemble measurement, the Z-average diameter obtained for a polydisperse population is skewed in favor of the larger objects due to their stronger scattering intensity.

Cryo-TEM of the CNC suspensions was used to confirm that the observed morphologies were not due to imaging artefacts arising from drying during conventional TEM sample preparation.<sup>[23]</sup> In the cryo-TEM images, **C0** and **C3** appear laterally associated with rare occurrences of irregular composite particles, whereas **C3-Ca** exhibits significantly more irregular objects (see **Figure 1** and **Figure S7**). As such, these observations qualitatively validate the divergence of morphology between **C1-C3** and Ca-CNCs determined from the TEM analysis, with **C3-Ca** containing less elongated particles and more aggregates. These cryo-TEM observations also suggest that the aspect ratio of the Ca-CNCs measured by TEM particle analysis is overestimated, which could be caused by the capillary-induced alignment of the crystallites upon drying on the TEM grid.

## 2.4 Complementary Ensemble Characterizations

Viscosity measurements were used to complement the analysis of CNC morphologies from the TEM images. By performing viscosity measurements at various CNC concentrations in the dilute regime, we can estimate the shape factor ( $r$ ) of the CNCs in suspension (i.e. the “effective” 3D aspect ratio),<sup>[24]</sup> which provides an ensemble measurement that is exempt from drying artefacts. For each investigated sample, the measured relative viscosity ( $\eta_r$ ) as a function of the particle concentration  $c$  ( $\text{g mL}^{-1}$ ) was plotted in **Figure 3b**. The data was used to extract the intrinsic viscosity  $[\eta]$  ( $\text{mL g}^{-1}$ ) and the dimensionless Huggins coefficient ( $k_H$ ), which depends on object interactions, using the Huggins equation:<sup>[25]</sup>

$$\eta_r \approx 1 + [\eta]c + k_H[\eta]^2c^2 \quad (3)$$

This analysis revealed that **C3-Na** and **C0-Na** exhibited similar relative viscosity behavior, leading to close intrinsic viscosities ( $54 \pm 2$  and  $56 \pm 6$   $\text{mL g}^{-1}$  respectively) that are greater than that of **C3-Ca** ( $25 \pm 3$   $\text{mL g}^{-1}$ ), as summarized in **Table S9**.

The intrinsic viscosity  $[\eta]$  ( $\text{mL g}^{-1}$ ) can be used to estimate the CNC shape factor  $r$ . Assuming the CNCs can be modelled as prolate ellipsoids of shape factor  $r$  defined as their aspect ratio, the intrinsic viscosity is given by:<sup>[26,27]</sup>

$$[\eta] = \frac{8}{15} \frac{(r^4 - 1)}{\rho_{\text{CNC}} r^2 \left[ \frac{(2r^2 - 1) \cosh^{-1}(r)}{r\sqrt{r^2 - 1}} - 1 \right]} \quad (4)$$

where  $\rho_{\text{CNC}}$  is the CNC volumetric mass density (taken to be  $1.6$   $\text{g mL}^{-1}$ <sup>[28]</sup>). Both **C3-Na** and **C0-Na** have the same shape factor of 35, which is greater than the shape factor of 22 exhibited by **C3-Ca** (see **Table S9**). These results confirm a similarity of 3D shape between never-

centrifuged and centrifuged CNCs, while highlighting a lower aspect ratio for the Ca-CNCs, in accordance with the analysis from the TEM and cryo-TEM images.

The shape factor obtained by viscometry are significantly greater than the aspect ratios obtained from the analysis of TEM images. For charged CNCs, viscometry often lead to larger shape factor compared to the average aspect ratio obtained from TEM or AFM particle analysis.<sup>[24,29–31]</sup> A possible cause for this observation is the extrapolation from a 2D measurement to a 3D aspect ratio despite CNCs usually having anisotropic cross-sections, with thicknesses often two to three times smaller than their widths.<sup>[10]</sup> Another possible source of error could arise from the formation of larger composite particles due to capillary forces upon drying on the TEM or AFM grid, leading to an underestimation of the aspect ratio for the true population. Finally, this discrepancy can also be explained by the presence of electroviscous effects that cause a significant increase in apparent aspect ratio, when the measurements are performed without salt addition,<sup>[24,32]</sup> as was the case in this study.

The Huggins coefficients ( $k_H$ ) extracted from **Equation 3** are presented in **Table S9**. Both **C3-Na** and **C0-Na** exhibited similar  $k_H$  ( $0.5 \pm 0.1$  and  $0.1 \pm 0.2$  respectively), which are both distinctly lower than for **C3-Ca** ( $1.6 \pm 0.8$ ). All were in the range previously reported for CNCs,<sup>[33]</sup> and other comparable charged elongated nanoparticles.<sup>[34]</sup> The greater  $k_H$  displayed by **C3-Ca** indicates that Ca-CNCs displayed stronger mutual interactions (either repulsive or attractive). To investigate the origin of the differences in inter-particle interactions between samples, the surface potential of the CNCs was estimated by  $\zeta$ -potential measurements (**Table S1**). The absolute  $\zeta$ -potential for Ca-CNCs (approx. 35 mV) is lower than for Na-CNCs (approx. 43 mV), indicating that they have a lower colloidal stability than their parent samples. The evolution of the effective charge per particle as a function of the size presented in **Figure S1**, suggests that the lower absolute  $\zeta$ -potential of Ca-CNCs is not explained solely by a size increase, but rather by a lower effective charge (see Section **S1** of the Supporting Information for more details). Such a lower effective charge could be attributed to a lowering of the surface charge upon aggregation due to the burying of sulfate groups on the contact area between crystallites, or to a reduction of the effective surface charge due to the adsorption of tightly bound calcium cations at the CNC surface.<sup>[35]</sup>

Conductometric titration against sodium hydroxide showed that centrifuged (**C3**) and never-centrifuged CNCs (**C0**) exhibit the same surface charge per mass ( $264 \pm 5$  mmol kg<sup>-1</sup>), indicating that bundle formation did not cause a significant burying of surface sulfate groups. Consequently, the lowering of surface area upon centrifugation led to an increase of the surface charge per surface area of the CNCs (**Table S1**). Moreover, elemental analysis was used to estimate the amount of Ca<sup>2+</sup> ions in **C3-Ca**, which yielded a calcium content of 133 mmol kg<sup>-1</sup>, corresponding to half of the surface charges measured for its parent sample (**C3**) (**Table S1**). Given the divalent character of Ca<sup>2+</sup>, this corresponds to 266 meq kg<sup>-1</sup> of Ca<sup>2+</sup>, indicating that all the charged groups on the surface of **C3-Ca** were in the form of a calcium salt and that they were not hidden during the calcium-induced aggregation process. This charge coverage with Ca<sup>2+</sup> is consistent with the lower colloidal stability of Ca-CNCs compared to **C0-Na** and **C3-Na** and can be attributed to the screening of the surface charges by the metallic cations adsorbed onto the surface.<sup>[35]</sup>

## 2.5 Internal Structure of Composite Particles

While the previous morphological analyses only considered the nature of the relative alignment of the long axes of the crystallites within the composite particles, the relative orientation of the cross-section of the crystallites (i.e. with respect to their crystal structure) can have an important

impact on the CNC properties. In cotton fibers, native crystallites are mainly found in the cellulose I $\beta$  crystalline allomorph and are believed to possess approximately hexagonal cross-sections, as illustrated in **Figure 5a**.<sup>[36]</sup> Consequently, the vast majority of the exposed crystal surfaces corresponds to the (110) and (1-10) planes, with the remaining surfaces corresponding to the (100) plane. The greater density of hydroxy groups on the (110) and (1-10) planes is expected to make these faces more hydrophilic than the (100) plane, which is therefore described as “hydrophobic” by comparison. Previous studies have postulated that crystallites in bundle-like CNCs are preferentially associated along these hydrophobic faces.<sup>[9,12]</sup> This mechanism agrees with the preservation of the surface charge per mass upon bundle formation from **C0** to **C3**, as an association along the hydrophobic (non-charge-bearing) faces would maintain the exposed surface charges.

The relative orientation of the cross-section of the crystallites within composite CNCs cannot be determined by conventional morphological characterization such as TEM or AFM. We therefore characterized our samples using scanning nanobeam electron diffraction (SNBED), a method of four-dimensional scanning transmission electron microscopy (4D-STEM). This technique uses a focused electron beam to obtain the local 2D electron diffraction (ED) patterns for each position scanned across a TEM grid, as illustrated in **Figure 5b**.<sup>[37]</sup> Each ED pattern was collected by an electron beam probe with a diameter of 25 nm, with all crystallites within the probe diameter contributing to the obtained diffraction information. Each scan position containing an ED pattern (considered a “pixel”) was indexed according to the cellulose I $\beta$  unit cell.<sup>[38]</sup> This information was used to deduce the local crystallographic orientation with respect to the electron beam, as illustrated in **Figure 5b**. Example SNBED data is provided in **Figure S9**.

The CNC diffraction patterns could be divided into three distinct categories, corresponding to either the [010], [110] or [1-10] zone axes pointing normal to the TEM grid surface. None of the diffraction patterns corresponded to the [100] zone axis, which indicates that crystallites were never observed with their hydrophobic faces parallel to the grid. This is likely due either to poor adhesion between the hydrophobic (100) surface and the hydrophilic glow-discharged carbon film used for the TEM grid or to the cross-sectional anisotropy of the particles. The lack of observation of other crystallographic planes suggests the CNCs are relatively well-faceted in the planes corresponding to the observed zone axes. **Figure 5c** shows the relative amount of each crystallite orientation for each sample as a proportion of the SNBED pixels for which diffraction patterns were observed. For the never-centrifuged CNCs (**C0**), 44% of the measured pixels corresponded to the [010] zone axis (pointing normal to the TEM grid), with the remaining 56% divided between the [110] and [1-10] zone axes. In contrast, for the centrifuged CNCs (**C3**) and the Ca-CNCs (**C0-Ca** and **C3-Ca**), a strong majority of the measured pixels corresponded to the [010] zone axis (respectively 79%, 82% and 74%). These results indicate that for all the samples, the crystallites are not randomly oriented on the TEM grid, but rather lay more favorably with their (010) face in the plane of the grid.

The higher prevalence of the observed [010] orientation for **C3** compared to **C0** indicates that the preferential orientation of crystallites is enhanced upon bundle formation (**Figure 5c**). This observation cannot be fully explained by a potential favored interaction between a specific crystal face and the carbon supporting film on the TEM grid, as discussed in Section S5 of the Supporting Information. Instead, this prevalence likely results from a systematic increase of the cross-sectional anisotropy during bundle formation, which constrains the particle orientation upon landing on the grid surface. Such anisotropy would arise from a preferential association of the crystallites through a unique crystal face perpendicular to (010). Consequently, the

prevalence of the [010] zone axis suggests that the crystallites are preferentially associated through their hydrophobic (100) planes.

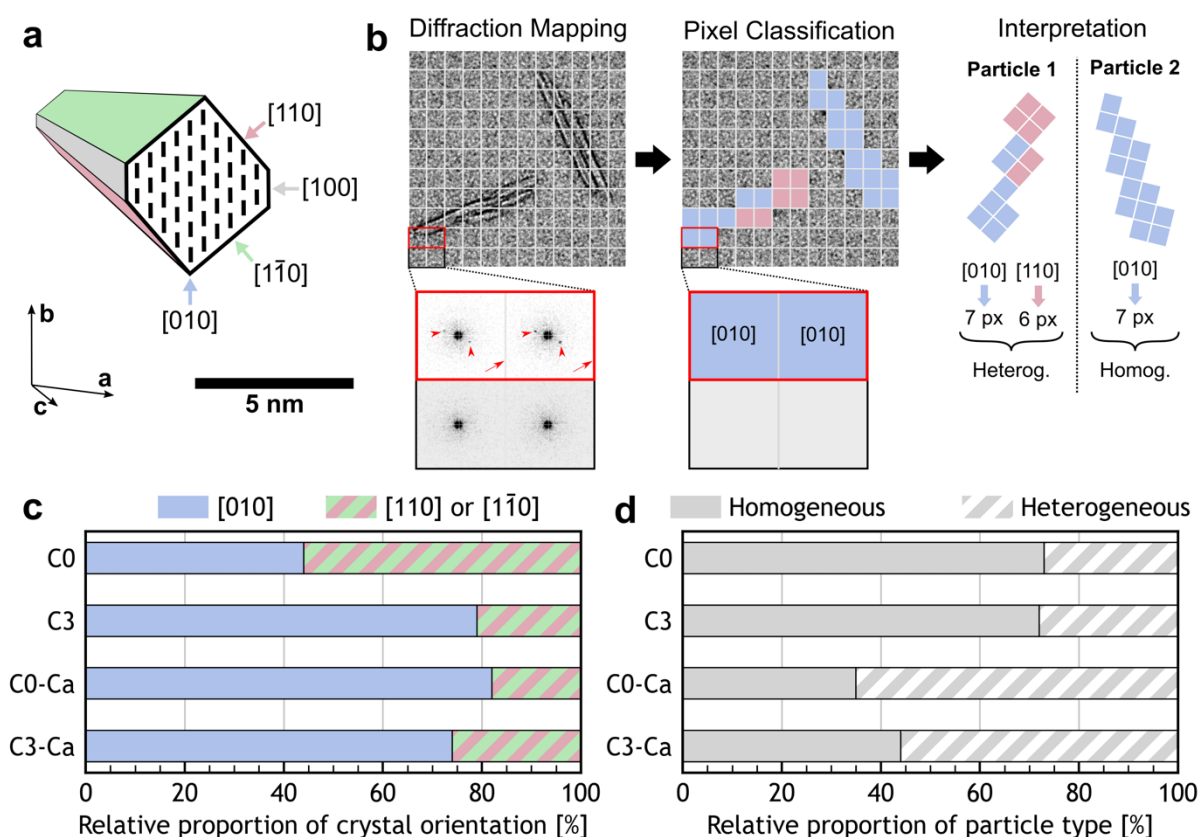


**Figure 5.** Local orientation of the crystallites constituting the cellulose nanocrystals probed by scanning nanobeam electron diffraction (SNBED). **(a)** Cross-section of native cellulose  $\beta$  crystal from cotton and indication of the crystal zone-axes directions (normal to their corresponding crystal plane). **(b)** Illustration of the diffraction pattern mapping process, with pixel classification (illustrative examples) according to crystal orientation ([010] in blue, [110] in pink or [1-10] in green), and particle classification with particles displaying a mix of crystal orientations classified as Heterogeneous (**Particle 1**) and pixels from particles displaying only one orientation classified as Homogeneous (**Particle 2**), the small squares have a dimension of 25x25 nm<sup>2</sup>. **(c)** Corresponding relative proportion of cellulose crystal plane orientations (based on pixel number) and **(d)** relative proportion of particle type.

The ED data was further analyzed to assess the heterogeneity of the crystalline orientations within individual CNCs. For this, the SNBED data was classified based on the number of extracted crystal orientations within an individual particle: particles composed of pixels categorized with different crystallographic orientations were classified as “Heterogeneous” (illustrated by the particle 1 in **Figure 5b**), while particles containing pixels categorized with only a single crystallographic orientation were classified as “Homogeneous” (illustrated by particle 2 in **Figure 5b**). The relative occurrence of each particle type is shown in **Figure 5d**. For the never-centrifuged (**C0**) and the centrifuged (**C3**) samples nearly three-quarters of the particles were Homogeneous (73 and 72% respectively), confirming that bundle-like CNCs are made of preferentially oriented crystallites. In contrast, much fewer Homogeneous particles

were observed for the Ca-CNCs (35 and 44% for **C0-Ca** and **C3-Ca**, respectively), which is consistent with these samples containing a large proportion of randomly associated crystallites.

Compared to their parent sample **C3**, the sample **C3-Ca** exhibited the same relative proportion of [010] zone-axis while mostly containing particles with heterogeneous crystal orientations (**Figure 5c** and **Figure 5d**). The retention of the prevalence of [010] orientation could be explained by the pre-existing raft-like CNCs present in **C3** imposing their orientation to the randomly associated particles. Yet, **C0-Ca** also exhibited a comparably high proportion of [010] orientations despite being made from **C0**, which contains fewer and smaller bundle particles (**Figure 5e**). Overall, this suggests that salt-induced aggregation of **C0** leads to the association of crystallites into irregular composite particles, but with a comparable reduction of exposed hydrophobic planes as in **C1-3**. This observation could indicate that salt-aggregation also leads to bundle formation, as also suggested by the behavior of CNC suspensions concentrated in the presence of NaCl (see **Figure S13** and the corresponding discussion in Section S7).

## 2.6 Cohesion Analysis

According to DLVO theory, irregular composite CNCs are less stable than laterally aligned CNCs.<sup>[18]</sup> Therefore, estimating the relative mechanical cohesion of the different samples could provide further evidence that their compositional arrangement is different. Mild ultrasonication (e.g. using a bath sonicator) is often used to redisperse loose CNC aggregates, with minor impact on the morphology of the crystallites.<sup>[2,39]</sup> However, significantly increasing the ultrasonication dose eventually leads to near complete fragmentation of the composite particles back into individual crystallites.<sup>[10,40]</sup> Consequently, ultrasonication is accompanied by a drastic reduction of the Z-average diameter of the CNCs,<sup>[10,13,41,42]</sup> which can be used to probe the relative strength of interaction between crystallites in the different types of composite particles.

The fragmentation of the CNCs with increasing ultrasonication dose ( $u$ ) was monitored by measuring the Z-average diameter ( $Z$ ) by DLS (**Figure 6a**). For all samples,  $Z$  decreases sharply with increasing  $u$ , as previously observed for CNCs.<sup>[10,13,41,42]</sup> Samples **C3** and **C0** displayed similar size decrease behavior, while ultrasonication had a greater impact on the size change of **C3-Ca** and **C0-Ca**. Consequently, despite having different starting sizes ( $Z^0$  at  $u = 0$ ), all samples reached a plateau of  $Z^\infty = 59 \pm 2$  nm for  $u > 445$  J mL<sup>-1</sup>. This result suggests that composite particles formed during calcium aggregation are less cohesive than the bundle-like particles. This is in accordance with the higher energetic configuration predicted by DLVO theory for crossed-associated CNCs compared to laterally associated CNCs.<sup>[18]</sup>

A quantitative analysis of the decay of the Z-average diameter with the sonication dose allows for the dissociation functions between the different samples to be distinguished. A simple dissociation process was initially considered and led to a biexponential fitting of the evolution of  $Z(u)$ , but this showed poor agreement with data at intermediate sonication doses (see **Figure S10**, **Table S10**, and the corresponding discussion in the Supporting Information). A better agreement with the data was instead obtained with a modified dissociation **Equation S15**, with a dose dependent factor  $k'(u)$ , which after integration yields:

$$Z(u) = [Z^0 - Z^\infty] \exp(-[k' u]^\alpha) + Z^\infty \quad (5)$$

where  $Z^\infty$  (nm), the Z-average diameter at infinite ultrasonication dose, was fixed to 59 nm for all samples. To independently isolate the dissociation of the composite particles formed during calcium-induced aggregation, the expression of the Z-average diameter of Ca-CNCs ( $Z_{Ca}$ , nm)

included the fitted Z-average diameter of their parent CNC sample  $Z(u)$  (i.e. **Equation 5**), to yield:

$$Z_{Ca}(u) = [Z_{Ca}^0 - Z^0] \exp(-[k_{Ca} u]^{\alpha_{Ca}}) + Z(u) \quad (6)$$

This expression assumes that the size reduction for calcium-induced composite particles is independent and simultaneous to the size reduction for the bundle particles. The best fitting parameters of **Equation 5** and **Equation 6**, reported in **Table S11**, were used to fit the data presented in **Figure 6**. For all samples, the model fitted the data very well for all sonication doses ( $R^2 \geq 0.99$ ,  $MSE \leq 6.4 \text{ nm}^2$ ). The constants  $k$  for **C0** and **C3** (0.03 and 0.04  $\text{mL J}^{-1}$ , respectively) were an order of magnitude smaller than their corresponding  $k_{Ca}$  for **C0-Ca** and **C3-Ca** (0.33 and 0.46  $\text{mL J}^{-1}$ , respectively). The  $\alpha$  coefficients for **C0** and **C3** were also similar (0.57 and 0.53, respectively) and slightly lower than the  $\alpha_{Ca}$  for **C0-Ca** and **C3-Ca** (0.66 and 0.74, respectively). This analysis confirms that the irregular composite particles made by calcium aggregation are easier to break apart than the laterally associated bundles.

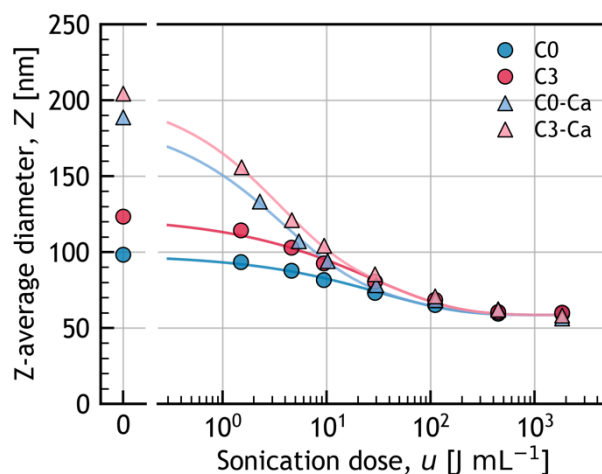


**Figure 6.** Impact of ultrasonication dose ( $u$ ) on the Z-average diameter ( $Z$ ) fitted using **Equations 5** and **6**.

## 2.7 Chiral Behavior

To determine whether the bundles formed by centrifugation display any enhanced chiral strength,<sup>[10]</sup> the liquid crystalline properties of the different CNCs were also compared. The anisotropic phase usually appears above a first threshold CNC concentration and increases with the CNC content until the suspension is fully cholesteric above a second threshold concentration. The volume fraction of anisotropic phase ( $\varphi_{ani}$ ) as a function of the CNC volume fraction ( $\Phi$ ) for **C0-Na**, **C3-Na** and **C3-Ca** is presented in **Figure 7a**. Compared to the never-centrifuged CNCs (**C0-Na**), the biphasic regime of **C3-Na** is narrower and shifted to lower concentrations. According to the Onsager model for achiral hard rods, this is indicative of rods having a larger aspect ratio,<sup>[43]</sup> which is in accordance with our morphological analyses indicating that centrifuged CNCs have an aspect ratio greater or equal to the never-centrifuged CNCs.

The pitch,  $p$ , defined as the distance over which the local orientation of CNCs within the cholesteric phase makes one full revolution around the helical axis, is known to decrease as the CNC volume fraction increases.<sup>[44,45]</sup> For cotton CNCs,  $1/p$  is found to be proportional to  $\Phi$ , which can be used to measure the strength of the chiral interactions between neighboring CNCs through the chiral strength ( $\kappa$ ,  $\mu\text{m}^{-1}$ ) expressed as:<sup>[46]</sup>

$$\frac{2\pi}{p} = \kappa \Phi \quad (7)$$

The evolution of the pitch as a function of the CNC volume fraction in **Figure 7b** reveals that **C3-Na** has a smaller pitch than **C0-Na**. The corresponding chiral strengths obtained by fitting **Equation 7** are  $26 \pm 1 \mu\text{m}^{-1}$  for **C0-Na** and  $44 \pm 2 \mu\text{m}^{-1}$  for **C3-Na**, confirming the stronger chiral interactions of the centrifuged CNCs. These observations are in accordance with the previously reported positive correlation between chiral strength and bundle proportion.<sup>[10]</sup> These results suggest that the additional centrifugation step leading to **C3-Na**, and commonly applied during the laboratory production of CNCs, is responsible for the formation of additional bundles that increase the effective left-handed chiral strength of the suspension and decrease the cholesteric pitch.

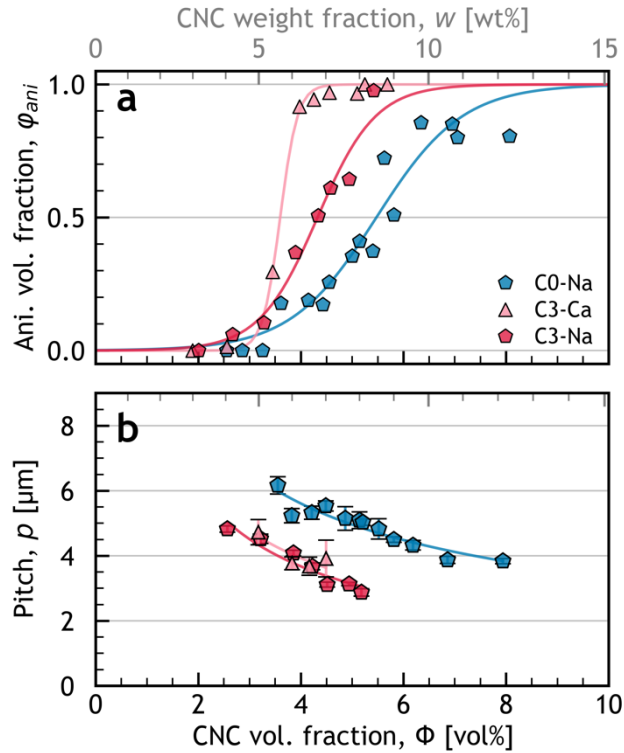


**Figure 7.** Liquid crystalline properties of different CNC suspensions: (a) anisotropic volume fraction ( $\varphi_{ani}$ ) and (b) pitch ( $p$ ) as a function of total CNC volume fraction ( $\Phi$ ) and weight fraction ( $w$ ) for **C0-Na** (blue circles), **C3-Na** (red circles) and **C3-Ca** (red triangles). Fitting lines are shown as a guide.

The interpretation of the evolution of the measured anisotropic volume fraction and pitch for **C3-Ca** is less straightforward. This sample exhibits a steep increase of  $\varphi_{ani}$  with increasing CNC volume fraction (**Figure 7a**), which can be indicative of early gelation. Between crossed

polarizers, this sample displays distinctive shear-alignment above 6 wt% (**Figure S12**), indicating that the sample is kinetically arrested (e.g. gelled) and was not able to relax over time, leading to an apparent  $\varphi_{ani}$  close to 100%. Such gelation at a low CNC volume fraction can be caused by the greater hydrodynamic volume induced by the irregular composite particles. Despite these clear signs of gelation, **C3-Ca** exhibited some fingerprint patterns arising from isolated tactoids, suggesting that local cholesteric ordering occurred in the transient stage between sample preparation and gelation.<sup>[2]</sup> The evolution of the pitch of these tactoids as a function of the CNC volume fraction followed the same trend as for **C3-Na**. This shows that some of the starting **C3-Na** CNCs remained unmodified upon calcium-induced aggregation, as suggested by their wide size distributions of length and width (**Figure 2c** and **Figure 2d**). Consequently, the Ca-CNCs retained the ability to form a cholesteric phase with the same chiral strength as their parent sample. Overall, these observations agree with the presence of irregular composite particles in the Ca-CNCs, which compromise their colloidal stability by promoting early gelation, but without clear modification of the overall chiral strength of the suspension.

Our results highlight the importance of CNC suspension history for their self-organization behavior. It is widely known that above a threshold ionic strength CNCs start to aggregate, leading to degradation of their self-organization ability while favoring gelation. Even though NaCl-induced aggregation of CNCs was thought to be reversible,<sup>[17]</sup> our experiments presented in **Figure 4** suggests otherwise. To illustrate this point, the self-assembly of CNC samples with different bundle content and ionic strength history was investigated. The results, presented in **Figure S13** highlight that exposure to ionic strength during capillary preparation can have irreversible consequences on the CNC self-assembly and size, probably arising from the irreversible formation of bundles (see discussion in Section **S7** of the Supporting Information for more details).

### 3. Conclusions

CNC morphology and size were tuned by modifying the post-hydrolysis purification protocol. Specifically, the first centrifugation step applied in most CNC extraction protocols at the laboratory scale was shown to be responsible for the formation of additional CNC “bundles” with raft-like morphology. These raft-like particles resulted from the preferential lateral association of crystallites through their hydrophobic faces, which occurs without screening the surface half-ester charges. The resulting CNC suspension displayed enhanced chiral strength with direct impact on its chiral liquid crystalline behavior. Moreover, the lower proportion of hydrophobic surfaces exhibited by these CNCs is expected to influence their surface properties, most notably their amphiphilicity.<sup>[47]</sup>

Aggregation of purified CNCs by exposure to calcium chloride at high ionic strength was also used to irreversibly increase the particle size in a controllable fashion. After dialysis, the obtained CNCs were in the form of calcium salts and exhibited a clear increase of the proportion of composite particles with an irregular morphology. Due to their high hydrodynamic volume, these irregular composite particles promoted gelation at a lower volume fraction, which could be of interest in applications, such as CNC-based rheological modifiers or nanocomposites.

The promoted formation, after the hydrolysis step, of bundles enhancing the chiral behavior of suspensions prompts some discussion about the origin of the chiral character of the CNCs. It is known that cellulose fibers often display a chiral arrangement in the plant cell walls,<sup>[48]</sup> and that

transient drying treatments, as it occurs in a flowering cotton bud prior to the harvest, leads to irreversible aggregation of the fibers upon water removal (i.e. hornification).<sup>[49]</sup> Consequently, it is *a priori* possible that the bundles driving the chiral collective behavior of the CNCs inherited from the chiral arrangement of aggregated cellulose fibers in the original plant tissue. However, the present work suggests otherwise, since bundles of higher chiral strength were produced artificially.

In conclusion, our results highlight how disregarded variations in the CNC extraction protocol can be critical in terms of suspension behavior. Importantly, while these findings are based on the analysis of CNCs obtained from sulfuric acid hydrolysis of cotton, they might be applicable to different sources and methods. This prompts further investigations, such as using CNCs extracted from wood or obtained by other production methods, which also typically display a dominant proportion of bundled particles.<sup>[6,8,50,51]</sup> This is especially important to consider for the use of commercial CNCs, which, unlike laboratory-made CNCs, are often purified by ultrafiltration instead of centrifugation,<sup>[52]</sup> and thus impact their particle morphology and colloidal properties. As such, this work pinpoints previously unexplored possibilities with immediate practical manufacturing considerations for commercial applications of CNCs, where their chiral liquid crystalline properties or their amphiphilicity are directly exploited, but also in any other situation where the CNC morphology and surface chemistry are key.

#### 4. Experimental Section

*Materials:* Sulfuric acid ( $\text{H}_2\text{SO}_4$ ,  $\geq 95\%$ , analytical grade), sodium hydroxide (NaOH, 99%, pellets), sodium chloride (NaCl,  $\geq 99.5\%$ , laboratory grade), calcium chloride ( $\text{CaCl}_2$ , fused granular) and hydrogen peroxide ( $\text{H}_2\text{O}_2$ ,  $> 30$  w/v%, laboratory reagent grade) were provided by Fisher Scientifics. All deionized water used in this work was type 1 ultrapure water (milli-Q, Millipore, Synergy UV system).

*Data processing* was performed with custom-made Python script. Statistical analysis and data fitting were performed with the Scipy library. The presented error on the fitting parameters corresponds to their standard deviation error calculated from the covariance matrix (pcov).

*CNCs suspensions* were produced by sulfuric acid hydrolysis of cotton derived filter paper (Whatman No. 1). Shredded filter paper (15 g, CookWork coffee grinder) was introduced in a 64 wt% sulfuric acid solution (300 g,  $\rho = 1.543 \text{ g mL}^{-1}$ ) preheated to 60 °C. After 30 min of hydrolysis under vigorous mechanical stirring, the medium was quenched with ice-cold water (300 mL). Part of the mixture was centrifuged (20,000 g, 20 min, 4 °C, Lynx 6000 Thermo Scientific) and the resulting pellet redispersed in water. This process was repeated to produce aliquots of CNCs that had never been centrifuged (**C0**), centrifuged once (**C1**), twice (**C2**), and three times (**C3**). All samples were dialyzed against deionized water (MWCO 12-14 kDa, Medicell membrane), with the water changed at least once a day until the conductivity was stable (around 2 weeks).

*CNC mass fraction* was obtained from gravimetric analysis by drying the suspensions in an oven (65 °C,  $> 40$  h). The mass of dry CNC was at least 15 mg and measurements were made in triplicate.

*CNC surface charge* was obtained from conductometric titration of CNC suspensions diluted in water (approx. 180 mL) in the presence of NaCl (0.2 mmol). An automatic titrator (Metrohm,

800 Dosino) was used to inject NaOH solution (10 mM Titripur®, 50  $\mu\text{L min}^{-1}$ ) while monitoring the conductivity (856 conductivity module). The CNC surface charge was deduced from the first equivalence point.

*Concentrated suspensions* of **C[n]-Na** were prepared by neutralizing the suspensions with 1 molar equiv. of NaOH per effective CNC charge followed by concentrating with a rotavapor (35 °C, 20 mbar), Ca-CNC samples were further concentrated by evaporation under ambient conditions and at room temperature.

*Calcium aggregated suspensions* of **C[n]-Ca** were obtained by preparing 6.5 wt% CNC suspensions of **C[n]-Na** containing  $\text{CaCl}_2$  ( $13.2 \pm 0.2$  mM), followed by a process of centrifugation (10,000 g, 20 min), redispersion (to approx. 1 wt% CNC), and dialysis against water ( $\geq 2$  weeks).

*Salt-induced aggregates* (**C[n]-Na, NaCl** and **C[n]-Na, CaCl<sub>2</sub>**) were prepared by diluting concentrated CNC suspension in water before pipetting  $\text{CaCl}_2$  or NaCl aqueous solution to form a 2 – 6.5 wt% CNC suspension in an ionic strength of 0 to 80 mM. The mixture was centrifuged (10,000 g, 20 min, Minispin Eppendorf), redispersed, then diluted for Zetasizer Measurements measurement as described below. The ionic strength of the CNCs, due to their surface ions, was not taken into account.

*Calcium content* was measured by inductively coupled plasma-optical emission spectrometry (ICP-OES, Thermo Fisher Scientific iCAP 7400 Duo ICP Spectrometer). Freeze-dried CNCs (~ 20 mg) were further dried overnight in an oven (60 °C). The precisely weighed CNCs were digested for 1 h in freshly prepared piranha solution (3:1 v/v  $\text{H}_2\text{SO}_4:\text{H}_2\text{O}_2$ ). A known amount of the mixture was diluted in water to obtain a solution of known concentration (approx. 3.6 wt% acid, approx. 2 g  $\text{L}^{-1}$  CNCs) that was used for the measurement. ICP Standard (Sigma-Aldrich) were diluted with approx. 2% nitric acid (TraceMetal™ Grade, Fisher) in water (TraceSelect™ for Trace Analysis, Honeywell Riedel-de Haen™) to make the standard curve. Analysis performed on Qtegra software.

*Zetasizer Measurements* were performed on dilute CNC suspensions (0.1 wt%), NaCl was used to set the ionic strength as close as possible to 1 mM. The Z-average diameters were estimated in backscattering geometry (173°, 633 nm, Malvern Zetasizer Nano ZS) from three runs of ten measurements after an initial waiting time of 5 min for the temperature to equilibrate (20 – 22 °C). The zeta potential was acquired after the Z-average measurement, through three runs of ten measurements and analyzed using the Smoluchowski equation. Data are presented as mean  $\pm$  standard deviation.

*TEM* was performed with a Talos F200X G2 microscope (FEI, 200 kV, CCD camera). A drop of CNC suspension (0.002 wt%, in 1 mM NaCl) was deposited on a glow-discharged carbon-coated copper grid. After 2 min, the excess solution was blotted with filter paper. Then, a drop of uranyl acetate aqueous solution (2 wt%) was deposited and let to sit for 1.5 min before blotting again. Particles ( $N \geq 225$ ) were manually outlined using Fiji (ImageJ), with all touching objects considered as a discrete CNC particle. Outlines were processed using the Shape Filter plugin to extract the bounding box length ( $L_b$ ), width ( $W_b$ ), and the particle area ( $A$ ).<sup>[53]</sup> The bounding box aspect ratio ( $r_b$ ) and rectangularity (*Rect*) were calculated from **Equation 1** and **Equation 2** respectively. Values were compared using a Mann–Whitney U test, for more details see Section S3 of the Supporting Information.

*Cryo-TEM* was performed using a JEOL JEM 2100Plus (Jeol, Japan), operated at 200 kV, equipped with a Gatan RIO 16 camera (Gatan Inc., U.S.A.). Cryo-frozen samples were prepared

using an EM GP2 Automatic Plunge Freezer (Leica microsystem, Germany) to vitrify the sample by rapid immersion in liquid ethane. The images presented were contrast enhanced to highlight the CNCs.

*SNBED* data were acquired in a low-dose condition optimized for cellulose crystals as described previously,<sup>[54]</sup> using a JEOL 2100F operating at 200 kV equipped with a NanoMEGAS ASTAR system. The nanobeam configuration consisted of a converged electron probe of 25 nm. An ED pattern was recorded at every probe position using a Cheetah Medipix3 direct electron detector (manufactured by Amsterdam Scientific Instruments) with a 0.5 ms exposure time per probe position. The diffraction datasets were analyzed using a dedicated ASTAR<sup>®</sup> software to perform: (i) crystal orientation identification through correlation with templates (i.e. pre-computed theoretical patterns) and (ii) Virtual–Bright (VBF) and Virtual–Dark field (VDF) image reconstruction that consists of plotting the intensity fluctuations of the transmitted beam (VBF) and user-selected diffraction positions (VDF) over the scanned area.

*Ultrasonication* of dilute CNC solutions (30 – 40 mL, 0.1 wt% CNCs, 1 mM NaCl) was performed in an ice bath using a Fisherbrand Ultrasonic disintegrator (20 kHz,  $\emptyset = 12.7$  mm, pulses 2:1 sec On:Off, 40% amplitude). Samples were ultrasonicated for regular intervals of increasing time in between which aliquots were removed for analysis (1 mL). The dose received by each sample ( $\text{J mL}^{-1}$ ) was calculated for each step from ultrasonication time divided by the volume of the sample and multiplied by the true power delivered (20 W, measured by Parton *et al.*<sup>[10]</sup>).

*Liquid crystalline properties* were investigated by observations of CNC suspensions in glass capillaries. The capillaries (CM Scientific, ID =  $0.3 \times 6.0$  mm<sup>2</sup>) were filled with a series of suspension dilutions prior to sealing with nail varnish and marking the initial meniscus position (so that any evaporation could be accounted for). The anisotropic volume fraction and corrected concentration were measured from the analysis of images taken after two weeks and again after at least a further week to confirm that no further evolution occurred. The pitch was measured after two weeks using polarized optical microscopy. Images were recorded in brightfield transmission configuration using a Zeiss Axio microscope in Koehler illumination equipped with a 50x objective (Nikon T Plan SLWD, NA 0.4) and a CMOS camera (UI- 3580LE-C-HQ, IDS). At least four images were recorded at different locations in the anisotropic phase, with three pitch measurements performed per image ( $N \geq 12$ ).

*Relative viscosity* was calculated from flow time measurements at low particle concentration by using:

$$\eta_r = \frac{t\rho}{t_0\rho_0} \approx \frac{t}{t_0} \quad (8)$$

where  $t$  and  $t_0$  are the flow times of the suspension and of the solvent respectively and  $\rho$  and  $\rho_0$  are the densities of the suspension and the solvent respectively. Flow times were measured in triplicate with an Ubbelohde viscometer (Technico,  $0.05 \text{ cSt s}^{-1}$ ) in air at 20 °C. The flow time of water was estimated to be  $18.65 \pm 0.09$  s (measured five times in triplicate,  $N = 15$ ). The intrinsic viscosity, and the Huggins coefficient, were extracted by fitting the relative viscosity as a function of the CNC concentration according to **Equation 3** and the 3D aspect ratio of the samples was estimated from the intrinsic viscosity by using **Equation 4**. The choice of approach and equation derivation are described in more detail in Section S4 of the Supporting Information.

## **Acknowledgments**

This work was funded by: EPSRC CDT, Automated Chemical Synthesis Enabled by Digital Molecular Technologies EP/S024220/1 (K.B., A.L.); EPSRC Bio-derived and Bio-inspired Advanced Materials for Sustainable Industries EP/W031019/1 (K.B., R.P., B.F.P., S.V.); EPSRC EP/T517847/1 (T.P.); ERC Horizon 2022 Proof of Concept Grants (ID: 101082172) (R.P., S.V.); Hiroshima University WPI-SKCM<sup>2</sup> (B.F.P.) This project was cofounded by European Regional Development Fund via the project “Innovation Centre in Digital Molecular Technologies” (A.L.). JHL and YO acknowledge Agence Nationale de la Recherche (ANR grant number: ANR-21-CE29-0016-1) and Glyco@Alps (ANR-15-IDEX-02) for their financial support and the NanoBio-ICMG platform (FR 2607) for granting access to the electron microscopy facility. The authors would like to thank Dr. Heather Greer (University of Cambridge) for her general help in acquiring the TEM images (thanks to the EPSRC underpinning multi-user equipment call. EP/P030467/1 grant). We also want to thank Dr Nigel Howard (University of Cambridge) for the ICP-OES measurements.

## **Supporting Information**

Supporting Information is joined at the end of the manuscript.

## **Conflict of Interest**

The authors declare no financial conflicts of interest.

## References

- [1] R. F. Nickerson, J. A. Habrle, *Ind. Eng. Chem.* **1947**, *39*, 1507.
- [2] B. Frka-Petesic, T. G. Parton, C. Honorato-Rios, A. Narkevicius, K. Ballu, Q. Shen, Z. Lu, Y. Ogawa, J. S. Haataja, B. E. Droguet, R. M. Parker, S. Vignolini, *Chem. Rev.* **2023**, *123*, 12595.
- [3] S. J. Eichhorn, A. Etale, J. Wang, L. A. Berglund, Y. Li, Y. Cai, C. Chen, E. D. Cranston, M. A. Johns, Z. Fang, G. Li, L. Hu, M. Khandelwal, K.-Y. Lee, K. Oksman, S. Pinitsoontorn, F. Quero, A. Sebastian, M. M. Titirici, Z. Xu, S. Vignolini, B. Frka-Petesic, *J. Mater. Sci.* **2022**, *57*, 5697.
- [4] O. M. Vanderfleet, E. D. Cranston, *Nat. Rev. Mater.* **2021**, *6*, 124.
- [5] B. G. Rånby, *Discuss. Faraday Soc.* **1951**, *11*, 158.
- [6] G. Delepierre, O. M. Vanderfleet, E. Niinivaara, B. Zakani, E. D. Cranston, *Langmuir* **2021**, *37*, 8393.
- [7] M. S. Reid, M. Villalobos, E. D. Cranston, *Langmuir* **2017**, *33*, 1583.
- [8] S. Elazzouzi-Hafraoui, Y. Nishiyama, J.-L. Putaux, L. Heux, F. Dubreuil, C. Rochas, *Biomacromolecules* **2008**, *9*, 57.
- [9] M. Uhlig, A. Fall, S. Wellert, M. Lehmann, S. Prévost, L. Wågberg, R. Von Klitzing, G. Nyström, *Langmuir* **2016**, *32*, 442.
- [10] T. G. Parton, R. M. Parker, G. T. van de Kerkhof, A. Narkevicius, J. S. Haataja, B. Frka-Petesic, S. Vignolini, *Nat Commun* **2022**, *13*, 2657.
- [11] F. Cherhal, F. Cousin, I. Capron, *Biomacromolecules* **2016**, *17*, 496.
- [12] C. Bruel, S. Queffeuilou, P. J. Carreau, J. R. Tavares, M.-C. Heuzey, *Langmuir* **2020**, *36*, 12179.
- [13] A. Brinkmann, M. Chen, M. Couillard, Z. J. Jakubek, T. Leng, L. J. Johnston, *Langmuir* **2016**, *32*, 6105.
- [14] T. Phan-Xuan, A. Thuresson, M. Skepö, A. Labrador, R. Bordes, A. Matic, *Cellulose* **2016**, *23*, 3653.
- [15] S. Kratochvil, G. E. Janauer, E. Matijević, *J. Colloid Interface Sci.* **1969**, *29*, 187.
- [16] M. Chau, S. E. Sriskandha, D. Pichugin, H. Thérien-Aubin, D. Nykypanchuk, G. Chauve, M. Méthot, J. Bouchard, O. Gang, E. Kumacheva, *Biomacromolecules* **2015**, *16*, 2455.
- [17] M. S. Reid, S. A. Kedzior, M. Villalobos, E. D. Cranston, *Langmuir* **2017**, *33*, 7403.
- [18] P. A. Buining, A. P. Philipse, H. N. W. Lekkerkerker, *Langmuir* **1994**, *10*, 2106.
- [19] Y. Boluk, L. Zhao, V. Incani, *Langmuir* **2012**, *28*, 6114.
- [20] H. Fukuzumi, R. Tanaka, T. Saito, A. Isogai, *Cellulose* **2014**, *21*, 1553.
- [21] F. Cherhal, F. Cousin, I. Capron, *Langmuir* **2015**, *31*, 5596.
- [22] F. Cherhal, B. Cathala, I. Capron, *Nord Pulp Paper Res J.* **2015**, *30*, 126.
- [23] Y. Ogawa, Y. Nishiyama, K. Mazeau, *Cellulose* **2020**, *27*, 9779.
- [24] Y. Boluk, R. Lahiji, L. Zhao, M. T. McDermott, *Colloids Surf. A Physicochem.* **2011**, *377*, 297.
- [25] M. L. Huggins, *J. Am. Chem. Soc.* **1942**, *64*, 2716.
- [26] M. Doi, S. F. Edwards, *The Theory of Polymer Dynamics*, Clarendon Press., Oxford, **1986**.
- [27] H. Brenner, *Int. J. Multiph. Flow* **1974**, *1*, 195.
- [28] K. R. K. Iyer, P. Neelakantan, T. Radhakrishnan, *J. Polym. Sci. A-2 Polym. Phys.* **1968**, *6*, 1747.
- [29] R. Tanaka, T. Saito, H. Hondo, A. Isogai, *Biomacromolecules* **2015**, *16*, 2127.
- [30] Q. Wu, X. Li, Q. Li, S. Wang, Y. Luo, *Polymers* **2019**, *11*, 781.
- [31] Q. Wu, X. Li, S. Fu, Q. Li, S. Wang, *Cellulose* **2017**, *24*, 3255.
- [32] J. Li, J.-F. Revol, R. H. Marchessault, *J. Colloid Interface Sci.* **1996**, *183*, 365.
- [33] E. González-Labrada, D. G. Gray, *Cellulose* **2012**, *19*, 1557.

- [34] A. M. Wierenga, A. P. Philipse, *Colloids Surf. A Physicochem.* **1998**, *137*, 355.
- [35] T. Cao, M. Elimelech, *J. Colloid Interface Sci.* **2021**, *584*, 456.
- [36] M. Martínez-Sanz, F. Pettolino, B. Flanagan, M. J. Gidley, E. P. Gilbert, *Carbohydr. Polym.* **2017**, *175*, 450.
- [37] C. Ophus, *Microsc. Microanal.* **2019**, *25*, 563.
- [38] Y. Nishiyama, P. Langan, H. Chanzy, *J. Am. Chem. Soc.* **2002**, *124*, 9074.
- [39] R. H. Marchessault, F. F. Morehead, M. J. Koch, *J. Colloid Sci.* **1961**, *16*, 327.
- [40] R. Tanaka, T. Kuribayashi, Y. Ogawa, T. Saito, A. Isogai, Y. Nishiyama, *Cellulose* **2017**, *24*, 3231.
- [41] B. Zakani, S. Entezami, D. Grecov, H. Salem, A. Sedaghat, *Carbohydr. Polym.* **2022**, *282*, 119084.
- [42] Z. J. Jakubek, M. Chen, M. Couillard, T. Leng, L. Liu, S. Zou, U. Baxa, J. D. Clogston, W. Y. Hamad, L. J. Johnston, *J. Nanopart. Res.* **2018**, *20*, 98.
- [43] L. Onsager, *Annals of the New York Academy of Sciences* **1949**, *51*, 627.
- [44] C. Honorato-Rios, A. Kuhnhold, J. R. Bruckner, R. Dannert, T. Schilling, J. P. F. Lagerwall, *Front. Mater.* **2016**, *3*, 21.
- [45] S. Elazzouzi-Hafraoui, J.-L. Putaux, L. Heux, *J. Phys. Chem. B* **2009**, *113*, 11069.
- [46] P. G. de Gennes, in *The Physics of Liquid Crystals*, Oxford University Press, Oxford, **1998**.
- [47] I. Capron, O. J. Rojas, R. Bordes, *Curr. Opin. Colloid Interface Sci.* **2017**, *29*, 83.
- [48] Y. Habibi, L. A. Lucia, O. J. Rojas, *Chemical Reviews* **2010**, *110*, 3479.
- [49] J. M. B. Fernandes Diniz, M. H. Gil, J. A. A. M. Castro, *Wood Science and Technology* **2004**, *37*, 489.
- [50] S. Montanari, M. Roumani, L. Heux, M. R. Vignon, *Macromolecules* **2005**, *38*, 1665.
- [51] L. Chen, J. Y. Zhu, C. Baez, P. Kitin, T. Elder, *Green Chemistry* **2016**, *18*, 3835.
- [52] Z. Hao, W. Y. Hamad, P. Yaseneva, *J. Chem. Eng.* **2023**, *478*, 147160.
- [53] T. Wagner, H.-G. Lipinski, *J. Open Res. Softw.* **2013**, *1*, e6.
- [54] J. H. Lim, Y. Jing, S. Park, Y. Nishiyama, M. Veron, E. Rauch, Y. Ogawa, *J. Phys. Chem. Lett.* **2023**, *14*, 3961.
- [55] S. Bhattacharjee, *J. Control. Release.* **2016**, *235*, 337.
- [56] B. W. Yap, C. H. Sim, *J. Stat. Comput. Simul.* **2011**, *81*, 2141.
- [57] R. F. Fedors, *Polymer* **1979**, *20*, 225.
- [58] M. Bercea, P. Navard, *Macromolecules* **2000**, *33*, 6011.
- [59] G. Lenfant, M. C. Heuzey, T. G. M. van de Ven, P. J. Carreau, *Cellulose* **2015**, *22*, 1109.
- [60] M.-C. Li, Q. Wu, R. J. Moon, M. A. Hubbe, M. J. Bortner, *Adv. Mater.* **2021**, *33*, 2006052.
- [61] X. M. Dong, T. Kimura, J.-F. Revol, D. G. Gray, *Langmuir* **1996**, *12*, 2076.

## Supporting Information

### Tailoring the Morphology of Cellulose Nanocrystals via Controlled Aggregation

*Kévin Ballu, Jia-Hui Lim, Thomas G. Parton, Richard M. Parker, Bruno Frka-Petesic, Alexei A. Lapkin, Yu Ogawa\*, Silvia Vignolini\**

Kévin Ballu, Dr Richard M Parker, Dr Bruno Frka-Petesic, Prof Silvia Vignolini  
Yusuf Hamied Department of Chemistry, University of Cambridge, Cambridge CB2 1EW,  
United Kingdom.

Jia-Hui Lim, Dr Yu Ogawa  
University Grenoble Alpes, CNRS, CERMAV, 38000 Grenoble, France.

\* E-mail: [yu.ogawa@cermav.cnrs.fr](mailto:yu.ogawa@cermav.cnrs.fr)

Dr Thomas G Parton, Prof Silvia Vignolini  
Department of Sustainable and Bio-inspired Materials, Max Planck Institute of Colloids and  
Interfaces, 14476 Potsdam, Germany.

\* E-mail: [sv@mpikg.mpg.de](mailto:sv@mpikg.mpg.de)

Dr Bruno Frka-Petesic  
International Institute for Sustainability with Knotted Chiral Meta Matter (WPI-SKCM<sup>2</sup>),  
Hiroshima University, Hiroshima 739-8526, Japan.

Prof Alexei Lapkin  
Department of Chemical Engineering and Biotechnology, University of Cambridge, Cambridge  
CB3 0AS, United Kingdom

Prof Alexei Lapkin  
Innovative Center in Digital Molecular Technologies, Yusuf Hamied Department of Chemistry,  
University of Cambridge, Cambridge CB2 1EW, United Kingdom.

## S1. CNC Surface Properties

**Table S1.** Summary of CNCs surface characteristics: Z-average diameter,  $\zeta$ -potential, surface charge per CNC mass from titration measurements, corresponding surface charge per surface area, and calcium content from elemental analysis. The surface charge per surface area was calculated by considering CNC with a sphere morphology and a diameter equal to their measured Z-average diameter.

Sample	Z-average (nm)	$\zeta$ -potential (mV)	Surface charge (mmol kg <sup>-1</sup> )	Surface charge (e nm <sup>-2</sup> )	Ca content (mmol kg <sup>-1</sup> )
C0	99 ± 1	-48 ± 5	264 ± 5	4.2 ± 0.1	N/A
C1	129 ± 1	-50 ± 8	269 ± 5	5.6 ± 0.1	N/A
C2	127 ± 1	-49 ± 5	267 ± 5	5.5 ± 0.1	N/A
C3	124 ± 2	-50 ± 8	264 ± 5	5.3 ± 0.1	N/A
C0-Na	94 ± 1	-41 ± 4	N/A	N/A	N/A
C3-Na	114 ± 1	-44 ± 1	N/A	N/A	6
C0-Ca	189 ± 1	-35 ± 1	N/A	N/A	N/A
C3-Ca	216 ± 9	-35 ± 2	N/A	N/A	133

### Effective Charge by Zetametry

The zeta potential ( $\zeta$ , mV) values presented in this study were calculated from the electrophoretic mobility ( $\mu_e$ ) according to the Helmholtz-Smoluchowski equation:<sup>[55]</sup>

$$\zeta = \frac{\mu_e \eta}{\varepsilon_r \varepsilon_0}$$

where  $\eta$  is the viscosity and  $\varepsilon_r$  and  $\varepsilon_0$  are the relative and vacuum permittivity respectively. The electrophoretic mobility is expressed as:

$$\mu_e = \frac{V}{E} \quad (S1)$$

where  $V$  ( $\mu\text{m s}^{-1}$ ) is the particle velocity and  $E$  ( $\text{V cm}^{-1}$ ) is the strength of the applied electric field. Therefore, an increase in particle size could lead to a lower effective charge which is expected to lead to a decrease of the absolute electrophoretic mobility and therefore a decrease of the absolute  $\zeta$ -potential. To investigate if the origin of the lower  $\zeta$ -potential exhibited by the Ca-CNCs, the effective charge per CNC ( $q_{eff}$ , e) was calculated from the electrophoretic mobility and the DLS diffusion coefficient ( $D_t$ ,  $\mu\text{m}^2 \text{s}^{-1}$ ) according to:

$$q_{eff} = \left| \frac{\mu_e}{D_t} \right| \frac{k_b T}{e}$$

where  $k_b$  ( $1.381 \cdot 10^{-23} \text{ J K}^{-1}$ ) is the Boltzmann constant,  $T$  (K) is the temperature of the measurement and  $e$  ( $1.602 \cdot 10^{-19} \text{ C}$ ) is the elementary charge.

The effective charge per CNC  $q_{eff}$  as a function of the Z-average diameter  $Z$  for each sample is plotted in **Figure S1**. The samples **C0-C3** followed a similar evolution of  $q_{eff}$  with increasing  $Z$ , indicating that the increase of effective charge per CNC is proportional to the Z-average diameter when the surface charge per mass is constant and the CNCs are in their proton or sodium form. However, comparatively to their size, the effective charge per CNC for the Ca-CNCs was much lower. This result suggests that the lower absolute  $\zeta$ -potential of the Ca-CNCs is not only due to a change in size, but rather to a change in effective charge.

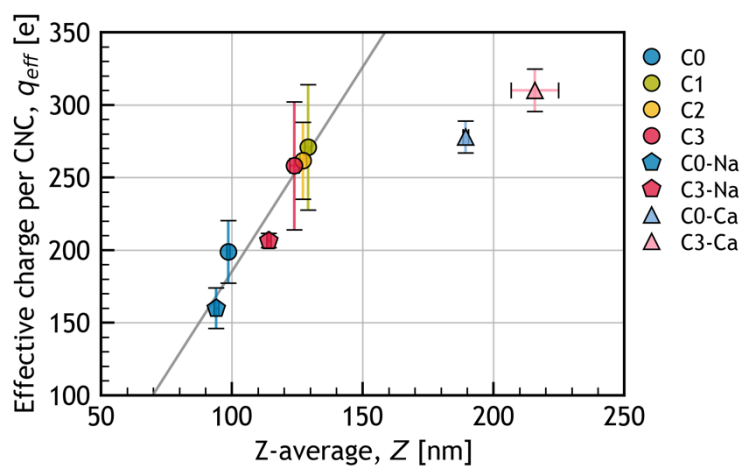


**Figure S1.** Evolution of the effective charge per CNC particle ( $q_{eff}$ ) as a function of the Z-average diameter ( $Z$ ) for all the samples.

## S2. Salt-induced CNC aggregation

### Influence of process parameters on salt-induced CNC aggregation

The impact of process parameters during the salt-induced aggregation of CNCs was investigated by DLS measurements. A CNC suspension of **C3-Na** was prepared with added  $\text{CaCl}_2$  to reach an ionic strength of aggregation  $I_{agg} = 51$  mM and a CNC weight fraction of aggregation  $w_{agg} = 6.5$  wt%. After a given time (0 h to 5 days) or centrifugation treatment (one or two 20 min cycles at 10,000 g), the suspension was redispersed and diluted in deionized water to a stable CNC suspension with  $w_{DLS} = 0.1$  wt% and at an ionic strength  $I_{DLS} = 1$  mM. The Z-average diameter of the resulting particles measured by DLS are presented in **Table S2**. In these conditions, the waiting time before redispersion and dilution seemed to have a negligible impact after 1 h. Similarly, applying any number of centrifugation cycles led to similar particle sizes, indicating that this does not influence the size of the particles after dilution. Consequently, the aggregation step of the following salt-induced aggregation experiments was carried out using one centrifugation cycle.

Using this approach, the CNC weight fraction during aggregation of **C3-Na** was varied ( $2.0 \leq w_{agg} \leq 6.5$  wt%) at fixed ionic strength ( $I_{agg} = 36$  mM). The resulting Z-average diameters are reported in **Figure S2**. Lowering the CNC mass fraction led to an increase of the particle size after aggregation from 243 to 311 nm. This effect could be due to the increase of viscosity upon increasing the CNC weight fraction. Therefore, the following aggregation experiments were all carried out with a fixed CNC weight fraction during aggregation of  $w_{agg} = 6.5$  wt%.

**Table S2.** Impact of the aggregation time ( $t_{agg}$ ) and number of centrifugation cycles ( $N_{centri}$ ) on the Z-average diameter (Z) of diluted CNCs after salt-induced aggregation of **C3-Na** at  $w_{agg} = 6.5$  wt% CNC and  $I_{agg} = 51$  mM of ionic strength induced by  $\text{CaCl}_2$  addition.

$t_{agg}$	$N_{centri}$	Z (nm)
0 h		$209 \pm 1$
1 h		$293 \pm 2$
3 h	0	$299 \pm 4$
24 h		$270 \pm 2$
196 h		$275 \pm 3$
N/A	1	$285 \pm 5$
	2	$274 \pm 2$
50 days	1	$274 \pm 6$

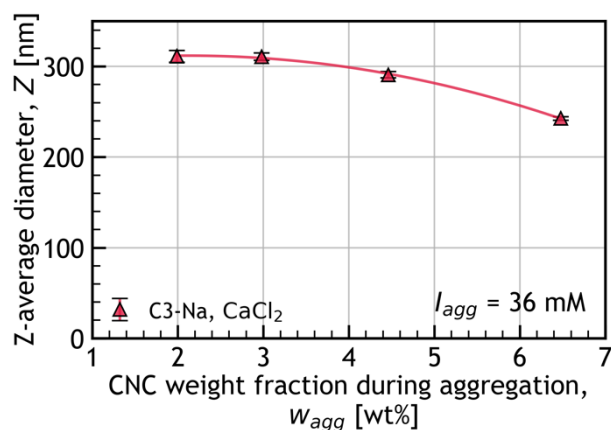


**Figure S2.** Evolution of the Z-average diameter ( $Z$ ) as a function of the CNC (**C3-Na**) mass fraction ( $w_{agg}$ ) during calcium aggregation at fixed ionic strength ( $I_{agg} = 26$  mM). The line of best fit, presented as a visual guide, was obtained from a second order polynomial.

The aggregation protocol presented in **Figure 4a** was followed to investigate the impact of the salt-type and ionic strength on the properties of the CNC suspensions and on their Z-average diameter after redispersion and dilution. We compared the impact of NaCl and CaCl<sub>2</sub> at various ionic strengths ( $0 \leq I_{agg} \leq 80$  mM) for both **C0-Na** and **C3-Na** ( $w_{agg} = 6.5$  wt%) on the properties of the suspension in two steps. First, after the aggregation step (i.e. after salt addition and centrifugation), leading to biphasic systems made up of a bottom birefringent arrested phase, and an upper clear liquid layer. Then, after redispersion and dilution to a stable CNC suspension with  $w_{DLS} = 0.1$  wt% and at an ionic strength ( $I_{DLS}$ ) as close as possible to 1 mM.

After the aggregation step, the bottom phase of the obtained aggregated CNC suspension was qualitatively inspected. For both salts, increasing the  $I_{agg}$  from 0 to 80 mM led to the formation of gels that required an increasing effort to be redispersed. The density of the arrested phase seemingly increased with increasing ionic strength, as visually indicated by its lower volume. Overall, these qualitative inspections indicate that for all salt types and CNC samples, increasing the ionic strength led to the formation of a stronger gel.

In the second step, the obtained CNC suspensions were redispersed, diluted and their Z-average diameter was measured. The time between sample centrifugation and their dilution for measurement varied from 0 to 63 days without significant impact on the Z-average diameter trend, as presented in **Figure S3**. The evolution of the Z-average diameter was highly dependent on the salt type and ionic strength, as illustrated in **Figure 4b**. Without salt addition, centrifugation did not modify the size of any of the samples (for comparison see **Figure 3a**). However, when sodium chloride was used to increase the ionic strength of never-centrifuged CNCs (**C0-Na, NaCl**), the suspension redispersed easily and a moderate size increase from  $\sim 100$  nm was observed only above 30 mM and quickly reached a plateau of  $\sim 145$  nm above 50 mM. In contrast, when calcium chloride was used to increase the ionic strength, a much stronger evolution of the size was observed for both never centrifuged and centrifuged CNCs (**C0-Na, CaCl<sub>2</sub>** and **C3-Na, CaCl<sub>2</sub>**). The Z-average diameter followed a sigmoidal evolution, starting to increase from approx. 100-120 nm at an ionic strength of 12 mM before reaching a plateau around 290 nm above 50 mM. Finally, increasing the ionic strength above 40 mM led to greater variability of the measured sizes around the overall trend ( $290 \pm 25$  nm), and small macroscopic gel particles could be visibly seen by the naked eye above 50 mM.

In comparison to  $\text{CaCl}_2$ , the moderate size reached after the addition of sodium chloride above a concentration threshold is surprising. Previous work has showed that  $\text{NaCl}$ -induced aggregation of centrifuged CNCs is reversible upon dialysis.<sup>[17]</sup> In our conditions, sample dilution leads to a dramatic reduction of the salt concentration, effectively mimicking the impact of dialysis on a CNC suspension. Consequently, we would expect the **C0-Na, NaCl** aggregates to be broken down into the starting CNC upon dilution, which should lead to a constant Z-average diameter. Instead, the Z-average diameter increased slightly and then reached a plateau at a size similar to **C3**, which could be indicative of the irreversible formation of bundles.

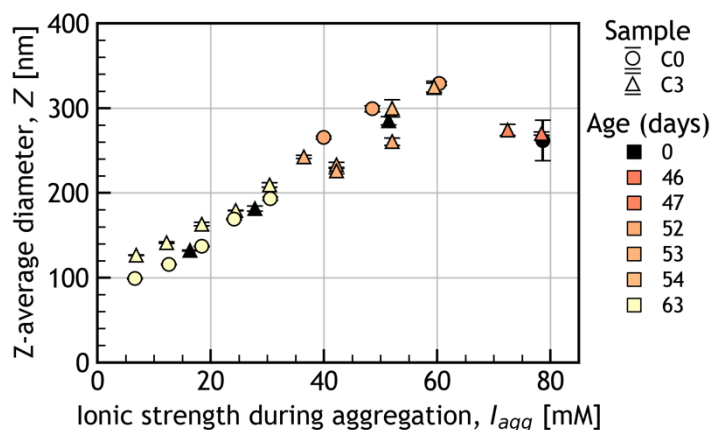


**Figure S3.** Evolution of the CNC Z-average size (Z) after dilution following calcium-induced aggregation as a function of ionic strength ( $I_{agg}$ ), CNC sample, and waiting time before dilution.

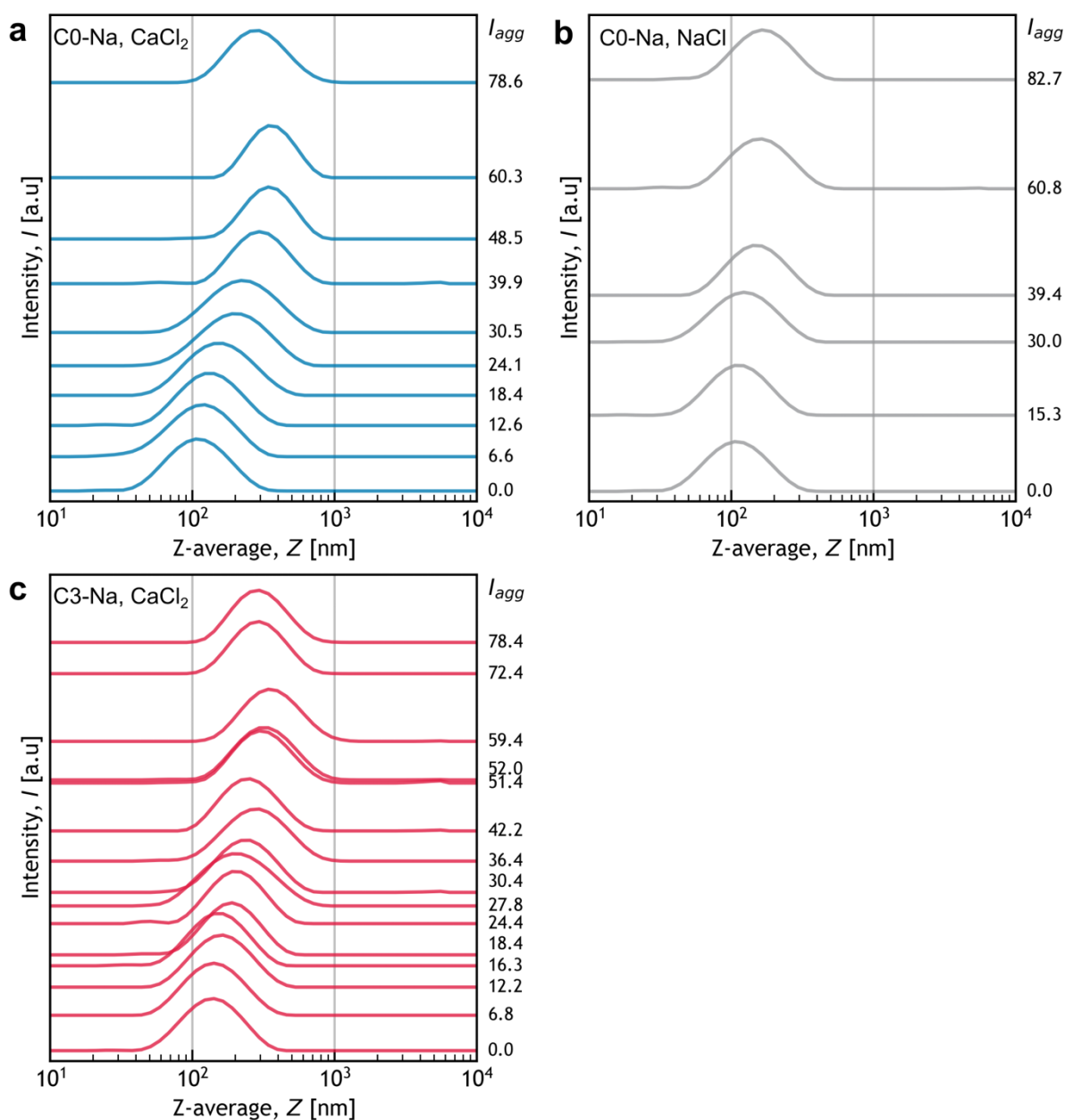


**Figure S4.** Evolution of the DLS scattered intensity ( $I$ ) as a function of the Z-average diameter ( $Z$ ) after dilution following salt-induced aggregation as a function of the ionic strength during aggregation ( $I_{agg}$ ) for **(a)** C0-Na with NaCl, **(b)** C0-Na with CaCl<sub>2</sub> and **(c)** C3-Na with CaCl<sub>2</sub>. Measurements were performed after redispersion and dilution to  $w_{DLS} = 0.1$  wt% and an ionic strength ( $I_{DLS}$ ) as close as possible to 1 mM.

### S3. TEM and Cryo-TEM analyses

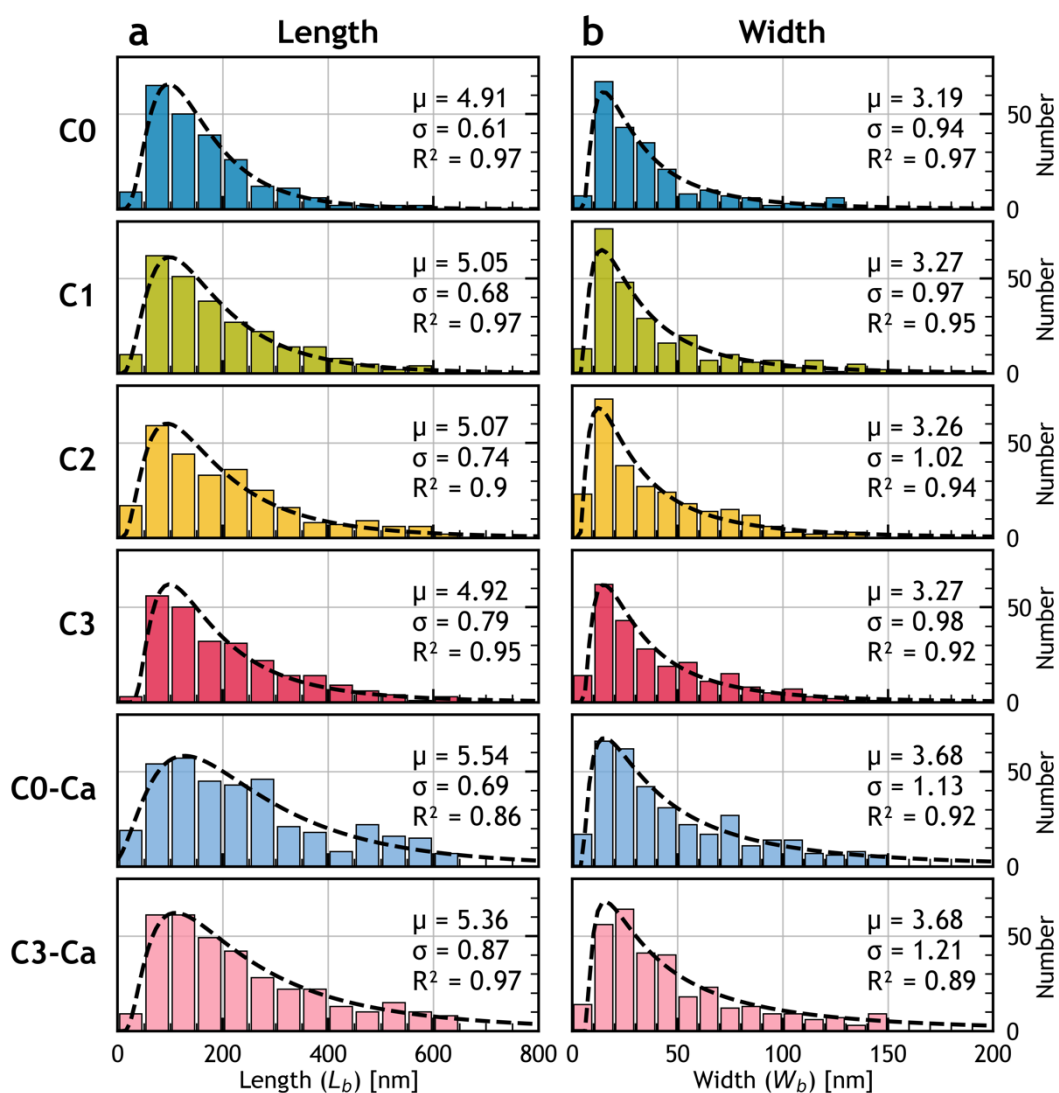


**Figure S5.** Histograms of CNC dimensions from analysis of TEM images (a) bounding box length ( $L_b$ ) and (b) bounding box width ( $W_b$ ). The data was fitted with a log-normal distribution and the corresponding fitting parameters are presented for each plot.

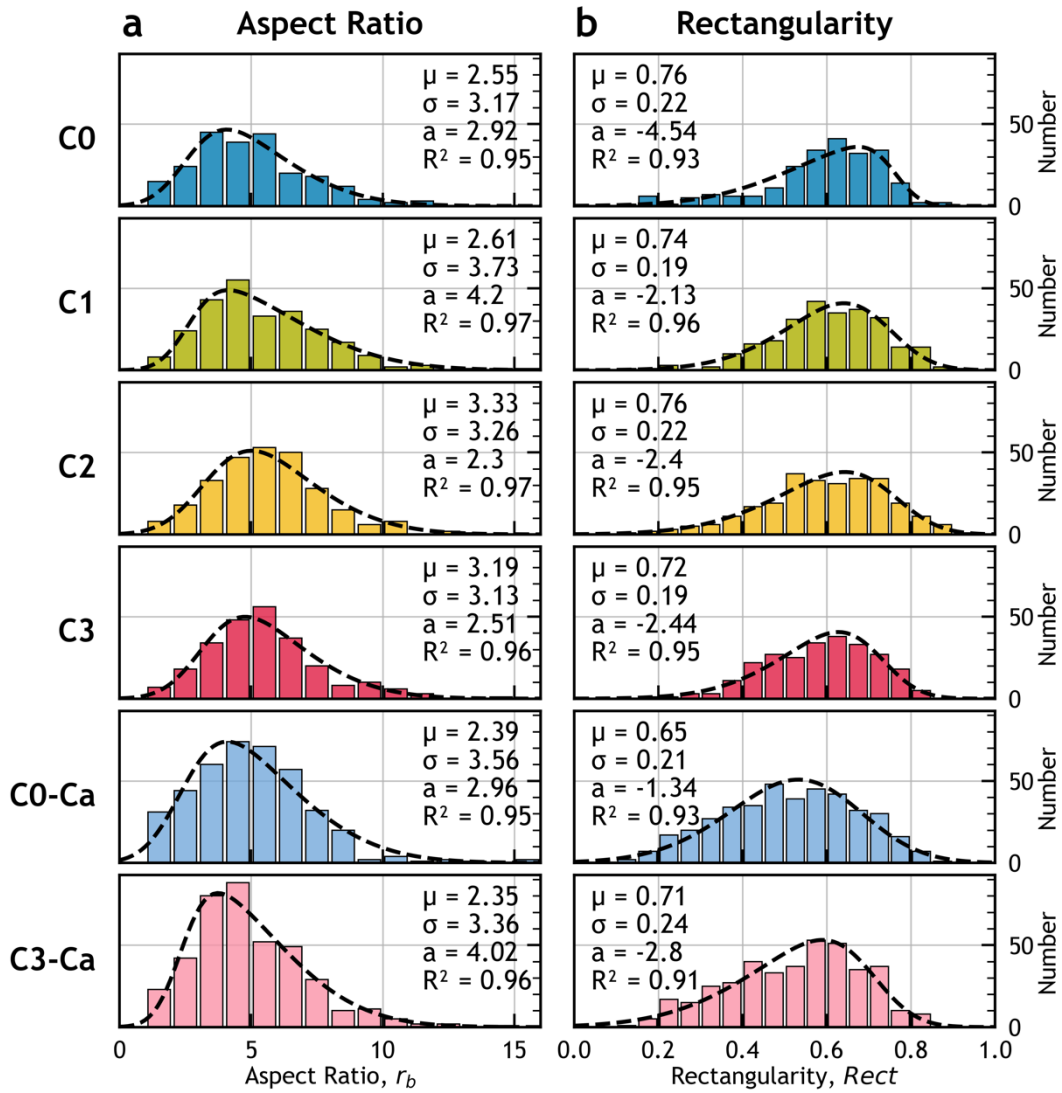


**Figure S6.** Histograms of CNC shape parameters from analysis of TEM images (a) bounding box aspect ratio ( $r_b$ ) and (b) rectangularity ( $Rect$ ). The data was fitted by skewed-normal distributions, the corresponding fitting parameters are presented for each plot.

### Statistical Analysis of TEM Values

The normality of the values obtained from TEM images was analyzed by applying a Shapiro–Wilk test on the logarithm of the bounding box lengths ( $L_b$ ) and bounding box widths ( $W_b$ ) and directly (without transformation of the data) on the corresponding bounding box aspect ratios ( $r_b$ ) and rectangularties ( $Rect$ ). The Shapiro–Wilk test compares the distribution of a dataset to a normal distribution through calculation of the statistic  $W$ ,  $\in [0;1]$ , for which a value of one indicates normality of the data, a corresponding p-value below the chosen confidence level indicates that there is evidence that the dataset is not normally distributed.<sup>[56]</sup> As presented in **Table S3**, most series did not follow a normal distribution with a confidence threshold of 0.05. Consequently, pairwise comparison of samples were performed using a Mann–Whitney U test, as it does not assume normality, the results for  $\ln(L_b)$ ,  $\ln(W_b)$ ,  $r_b$  and  $Rect$  are presented respectively in **Table S4**, **Table S5**, **Table S6** and **Table S7**.

**Table S3.** Shapiro–Wilk test of normality  $W$  statistic and corresponding  $p$ -values for the logarithm of the bounding box lengths ( $L_b$ ) and widths ( $W_b$ ) and for the aspect ratio ( $r_b$ ) and rectangularity ( $Rect$ ) for each sample (i.e. the  $p$ -value can be viewed as the probability to obtain these specific sample distributions if the corresponding population was normally distributed). The distribution of the data highlighted in red does not differ significantly from a normal distribution with a confidence threshold of 0.05.

Sample	$\ln(L_b)$	$\ln(W_b)$	$r_b$	Rect
<b>C0</b>	0.993 (0.346)	0.976 (0.001)	0.971 (0.000)	0.922 (0.000)
<b>C1</b>	0.992 (0.155)	0.977 (0.000)	0.933 (0.000)	0.983 (0.004)
<b>C2</b>	0.984 (0.005)	0.982 (0.002)	0.958 (0.000)	0.983 (0.003)
<b>C3</b>	0.982 (0.003)	0.984 (0.007)	0.967 (0.000)	0.984 (0.008)
<b>C0-Ca</b>	0.978 (0.000)	0.987 (0.001)	0.921 (0.000)	0.987 (0.001)
<b>C3-Ca</b>	0.993 (0.087)	0.980 (0.000)	0.952 (0.000)	0.979 (0.000)

**Table S4.** Mann–Whitney  $U$  statistics and corresponding  $p$ -value resulting from the pairwise comparison of  $\ln(L_b)$  for all samples. Data highlighted in red indicates that the corresponding samples do not differ significantly with a confidence threshold of 0.05.

	<b>C0</b>	<b>C1</b>	<b>C2</b>	<b>C3</b>	<b>C0-Ca</b>	<b>C3-Ca</b>
<b>C0</b>	/	26150 (0.043)	26352 (0.009)	23198 (0.001)	29887 (0.000)	28551 (0.000)
<b>C1</b>	26150 (0.043)	/	36022 (0.548)	30203 (0.246)	64522 (0.000)	64121 (0.000)
<b>C2</b>	26352 (0.009)	36022 (0.548)	/	32521 (0.573)	43106 (0.000)	65076 (0.000)
<b>C3</b>	23198 (0.001)	30203 (0.246)	32521 (0.573)	/	59359 (0.000)	58929 (0.000)
<b>C0-Ca</b>	29887 (0.000)	64522 (0.000)	43106 (0.000)	59359 (0.000)	/	80892 (0.601)
<b>C3-Ca</b>	28551 (0.000)	64121 (0.000)	65076 (0.000)	58929 (0.000)	80892 (0.601)	/

**Table S5.** Mann–Whitney U statistics and corresponding p-value resulting from the pairwise comparison of  $\ln(W_b)$  for all samples. Data highlighted in red indicates that the corresponding samples do not differ significantly with a confidence threshold of 0.05.

	<b>C0</b>	<b>C1</b>	<b>C2</b>	<b>C3</b>	<b>C0-Ca</b>	<b>C3-Ca</b>
<b>C0</b>	/	29136 (0.932)	30521 (0.995)	26244 (0.232)	34079 (0.000)	31567 (0.000)
<b>C1</b>	29136 (0.932)	/	34638 (0.852)	30388 (0.295)	64491 (0.000)	65298 (0.000)
<b>C2</b>	30521 (0.995)	34638 (0.852)	/	31518 (0.249)	41250 (0.000)	67829 (0.000)
<b>C3</b>	26244 (0.232)	30388 (0.295)	31518 (0.249)	/	59734 (0.000)	60494 (0.000)
<b>C0-Ca</b>	34079 (0.000)	64491 (0.000)	41250 (0.0)	59734 (0.000)	/	82229 (0.349)
<b>C3-Ca</b>	31567 (0.000)	65298 (0.000)	67829 (0.000)	60494 (0.000)	82229 (0.349)	/

**Table S6.** Mann–Whitney U statistics and corresponding p-value resulting from the pairwise comparison of  $r_b$  for all samples. Data highlighted in red indicates that the corresponding samples do not differ significantly with a confidence threshold of 0.05.

	<b>C0</b>	<b>C1</b>	<b>C2</b>	<b>C3</b>	<b>C0-Ca</b>	<b>C3-Ca</b>
<b>C0</b>	/	25842 (0.026)	24335 (0.000)	23612 (0.003)	44321 (0.613)	45203 (0.751)
<b>C1</b>	25842 (0.026)	/	37759 (0.112)	31092 (0.535)	47209 (0.043)	44161 (0.004)
<b>C2</b>	24335 (0.000)	37759 (0.112)	/	35444 (0.249)	63658 (0.000)	41610 (0.000)
<b>C3</b>	23612 (0.003)	31092 (0.535)	35444 (0.249)	/	43810 (0.009)	40510 (0.000)
<b>C0-Ca</b>	44321 (0.613)	47209 (0.043)	63658 (0.000)	43810 (0.009)	/	75991 (0.323)
<b>C3-Ca</b>	45203 (0.751)	44161 (0.004)	41610 (0.000)	40510 (0.000)	75991 (0.323)	/

**Table S7.** Mann–Whitney U statistics and corresponding p-value resulting from the pairwise comparison of *Rect* for all samples. Data highlighted in red indicates that the corresponding samples do not differ significantly with a confidence threshold of 0.05.

	<b>C0</b>	<b>C1</b>	<b>C2</b>	<b>C3</b>	<b>C0-Ca</b>	<b>C3-Ca</b>
<b>C0</b>	/	29011 (0.868)	31059 (0.730)	30278 (0.130)	59599 (0.000)	56521 (0.000)
<b>C1</b>	29011 (0.868)	/	33933 (0.557)	35008 (0.080)	34806 (0.000)	36449 (0.000)
<b>C2</b>	31059 (0.730)	33933 (0.557)	/	35385 (0.263)	70043 (0.000)	40067 (0.000)
<b>C3</b>	30278 (0.130)	35008 (0.080)	35385 (0.263)	/	36859 (0.000)	38548 (0.000)
<b>C0-Ca</b>	59599 (0.000)	34806 (0.000)	70043 (0.000)	36859 (0.000)	/	83112 (0.227)
<b>C3-Ca</b>	56521 (0.000)	36449 (0.000)	40067 (0.000)	38548 (0.000)	83112 (0.227)	/

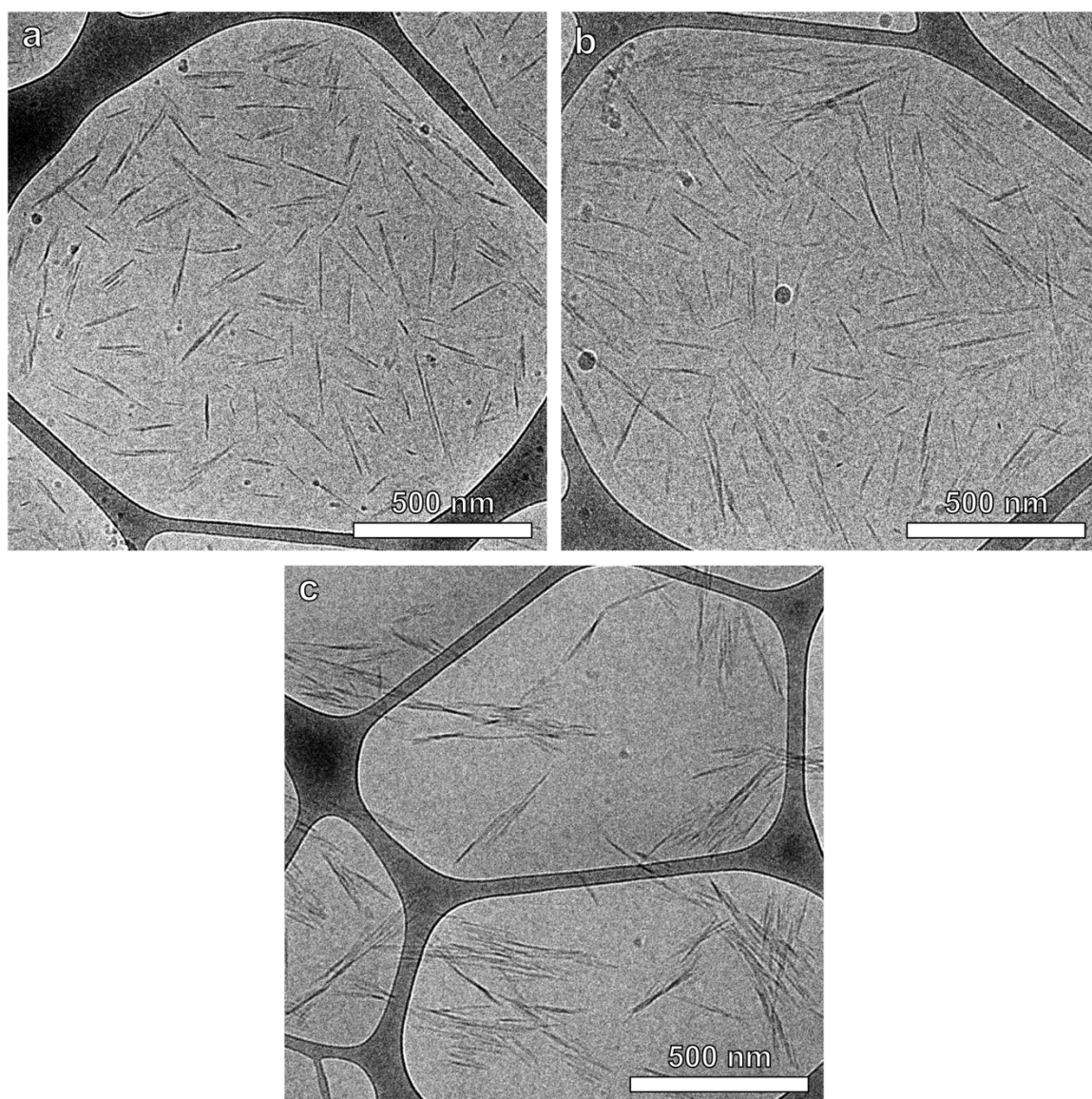


**Figure S7.** Typical images from Cryo-TEM of (a) never centrifuged CNCs (**C0**), (b) triply-centrifuged CNCs (**C3**) and (c) Ca-aggregated CNCs (**C3-Ca**).

## S4. Viscometry

### Fitting of the Relative Viscosity

In most previous studies, the intrinsic viscosity of CNC suspensions was obtained by fitting the data using a Fedors plot, according to the following expression:<sup>[24,29–31,33,57,58]</sup>

$$\frac{1}{2(\sqrt{\eta_r} - 1)} = \frac{1}{[\eta]c} - \frac{1}{[\eta]c_m} \quad (\text{S2})$$

where  $\eta_r$  and  $[\eta]$  are respectively the relative and intrinsic viscosities, and  $c$  and  $c_m$  are respectively the particle concentration and the concentration at maximum packing. However, this approach often yields physically incoherent (i.e. negative) critical concentrations,<sup>[59]</sup> which was also the case for our data, as illustrated in **Figure S8** and **Table S8**. The authors of the method recommend to neglect data points at low concentrations (i.e. below  $0.01 \text{ g mL}^{-1}$ ) as small uncertainties leads to huge change of  $\sqrt{\eta_r} - 1$ . However, in order to stay in the dilute regime, we did not measure the viscosity at such high concentrations. Therefore, we used the Huggins approach, presented in **Equation 3**, which does not suffer from this issue.

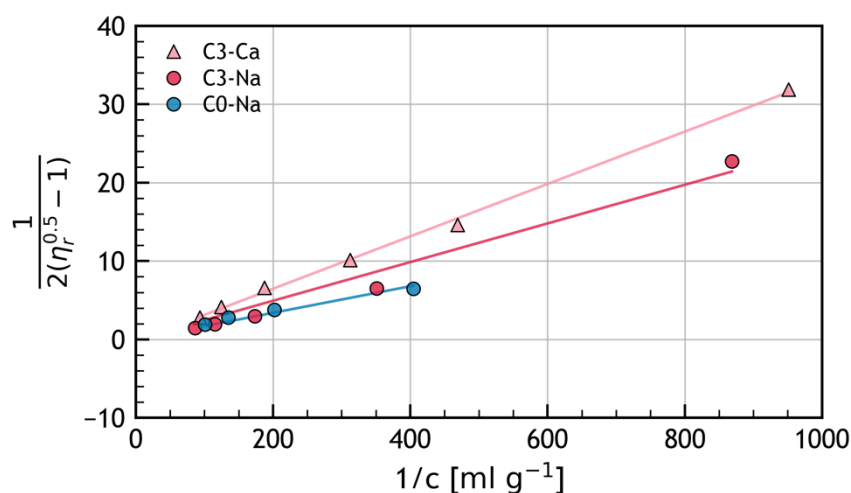


**Figure S8.** Fedors plot of the relative viscosity data. Values below  $0.001 \text{ g mL}^{-1}$  (i.e. above than  $1000 \text{ mL g}^{-1}$ ) were excluded.

**Table S8.** Results from the Fedors fit

Sample	$[\eta]$ (mL g <sup>-1</sup> )	$c_m$ (g mL <sup>-1</sup> )	R <sup>2</sup>
C0	59.0 ± 8.1	4.1E4 ± 5.6E10	0.95
C3	40.6 ± 4.6	-3.7E4 ± 6.6E10	0.97
C3-Ca	29.9 ± 0.7	0.2 ± 0.3	1.00

**Table S9.** Results from the Huggins fit

Sample	$[\eta]$ (mL g <sup>-1</sup> )	K <sub>H</sub>	R <sup>2</sup>
C0	56 ± 6	0.1 ± 0.2	0.99
C3	54 ± 2	0.5 ± 0.1	1.00
C3-Ca	25 ± 3	1.6 ± 0.8	0.99

### Expression for 3D Aspect Ratio

Various expressions for rods and spheroids can be used to relate the 3D aspect ratio ( $r$ ) to the intrinsic viscosity ( $[\eta]$ ), the Simha relation being the most widespread.<sup>[60]</sup> However, this expression is specific to rods and the CNC bundles in this work are closer in shape to a spheroid than a cylinder. Therefore, it is more appropriate to use an expression derived from Doi and Edwards, and Brenner for prolate spheroids,<sup>[26,27]</sup> for which the rotational friction constant is exactly resolved.

The intrinsic viscosity is defined as:

$$[\eta] = \lim_{c \rightarrow 0} \frac{1}{c} \frac{\eta - \eta_s}{\eta_s} \quad (\text{S3})$$

where  $\eta$  and  $\eta_s$  are the viscosities of the polymer and of the solvent respectively. In steady shear flow rate for rod-like polymers, the viscosity can be expressed as:<sup>[26]</sup>

$$\eta = \eta_s + \frac{2}{15} \frac{c}{\rho_p V_p} \zeta_{rot} \quad (\text{S4})$$

where  $c$  is the particle concentration,  $\rho_p$  is the particle density,  $V_p$  is the volume of a particle, and  $\zeta_{rot}$  is their rotational friction constant. According to Brenner,<sup>[27]</sup> the rotational friction constant can be expressed as:

$$\zeta_{rot} = 6\eta_s V_p K \quad (\text{S5})$$

where  $K$  is a dimensionless scalar coefficient defined in **Equation S7**. Consequently, from **Equation S3** to **S5**, the intrinsic viscosity can be simplified as:

$$[\eta] = \frac{4}{5} \frac{K}{\rho_{CNC}} \quad (\text{S6})$$

For spheroids:<sup>[27]</sup>

$$K = \frac{2(r^2 + 1)}{3(r^2\alpha_{\parallel} + \alpha_{\perp})} \quad (\text{S7})$$

with:

$$\alpha_{\perp} = \frac{r^2}{r^2 - 1}(1 - \beta) \quad (\text{S8})$$

$$\alpha_{\parallel} = \frac{2}{r^2 - 1}(r^2\beta - 1) \quad (\text{S9})$$

and where  $r$ , the 3D aspect ratio of the spheroid, is expressed as the ratio of its major axis over its minor axis. Finally, for prolate spheroids (i.e. with  $r > 1$ ):

$$\beta = \frac{\cosh^{-1}(r)}{r\sqrt{r^2 - 1}} \quad (\text{S10})$$

Finally, this yields **Equation 4**, as presented in the Results and Discussion section of the article.

## S5. Microelectron Diffraction

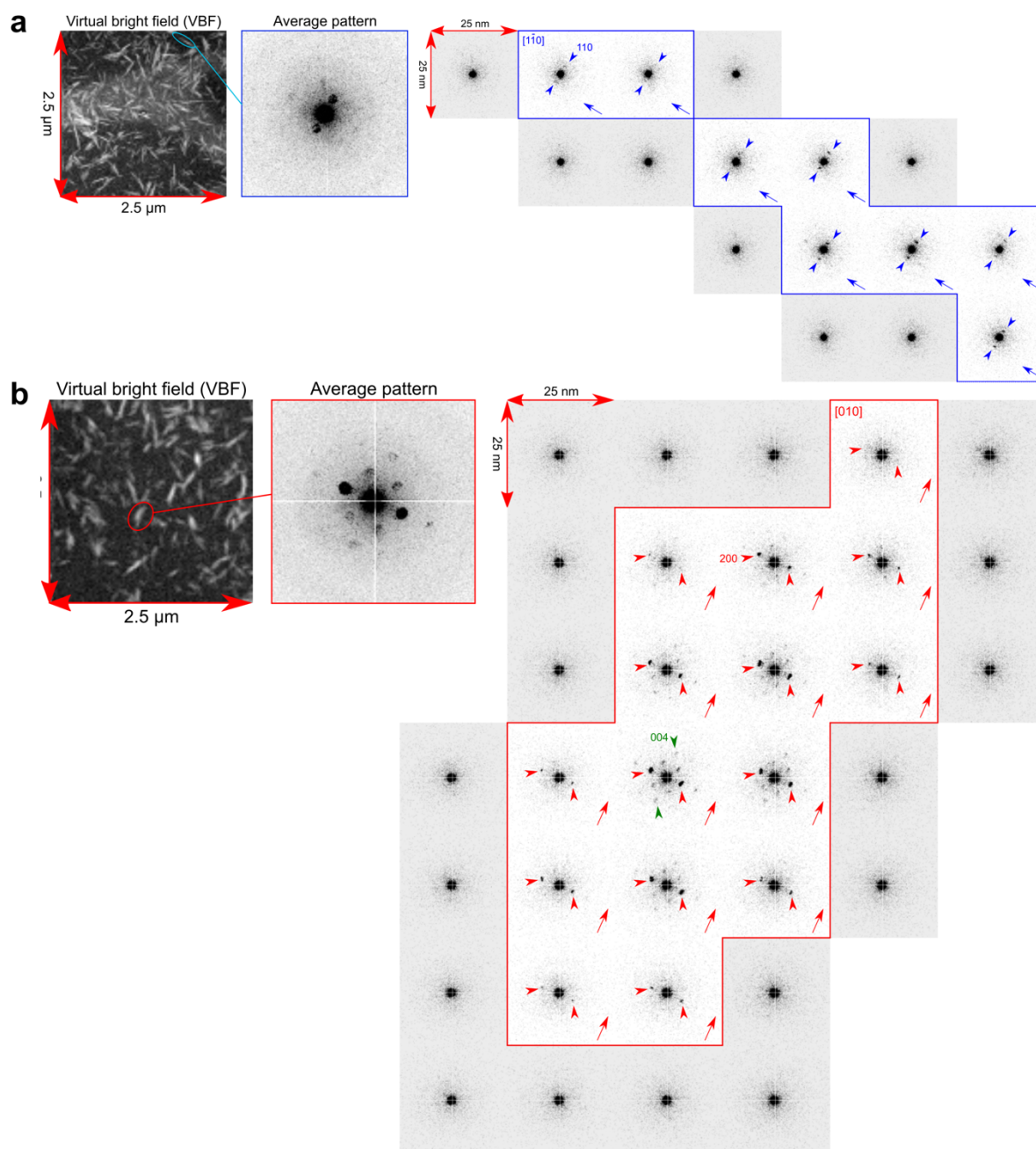


**Figure S9.** SNBED analysis with virtual bright field image (*left*), average diffraction pattern and ED patterns along a CNC (*right*) for (a) a never-centrifuged CNC (C0) displaying a [1-10] zone axis and (b) a centrifuged CNC (C3) displaying a [100] zone axis. The arrows on the corner of each ED pattern indicate the fiber axis.

### Impact of Favored Interaction between the Crystallites and the Grid

In a scenario where crystallite association would not be favored along any preferential crystal face, each crystal orientation on the grid would be equiprobable for any population of bundle

particles, and as such we would not observe a prevalent orientation. In such a case, even a preferential interaction between the (010) crystal faces and the carbon film on the grid would not account for the observed prevalence of [010] zone-axis orientation. Indeed, upon formation of bundle particles (i.e. from **C0** to **C3**), the (010) faces would be less available (as all the faces would be equally involved in the formation of bundles) resulting in a similar or lower proportion of observed [010] zone axis. Therefore, the sole prevalence of the observation of the [010] zone axis in bundled particles, because of how they lie flat onto the grid, also supports that there is a preferential association of the crystallites through their hydrophobic (100) planes.

## S6. Fitting the Z-average Diameter as a Function of Ultrasonication Dose

By relating the size change to a simple dissociation reaction, one can express an infinitesimal change of size ( $dZ$ ) as a function of an infinitesimal change of ultrasonication dose ( $du$ ) by using the rate equation:

$$\frac{dZ}{du} = -k Z \quad (\text{S11})$$

Where  $Z$  is the size and  $k$  is the rate of size change. This differential equation can be integrated into:

$$Z(u) = [Z^0 - Z^\infty] \exp(-k u) + Z^\infty \quad (\text{S12})$$

Considering that the dissociation of the calcium-aggregated objects occurs independently of the centrifuged CNCs, one can add a second term to express the size change of calcium-aggregated objects:

$$Z_{Ca}(u) = [Z_{Ca}^0 - Z^0] \exp(-k_{Ca} u) + [Z^0 - Z^\infty] \exp(-k u) + Z^\infty \quad (\text{S13})$$

which is equivalent to:

$$Z_{Ca}(u) = [Z_{Ca}^0 - Z^0] \exp(-k_{Ca} u) + Z(u) \quad (\text{S14})$$

Using this biexponential fitting approach, we extracted the rate of dissociation for the centrifuged CNCs and reused these to fit the size decrease of Ca-CNCs, as illustrated in **Figure S10a**. This method leads to reasonably good fitting of the data, as indicated by the high  $R^2$  and low MSE presented in **Table S10**, but the model misses some features at intermediate ultrasonication doses (**Figure S10b**).

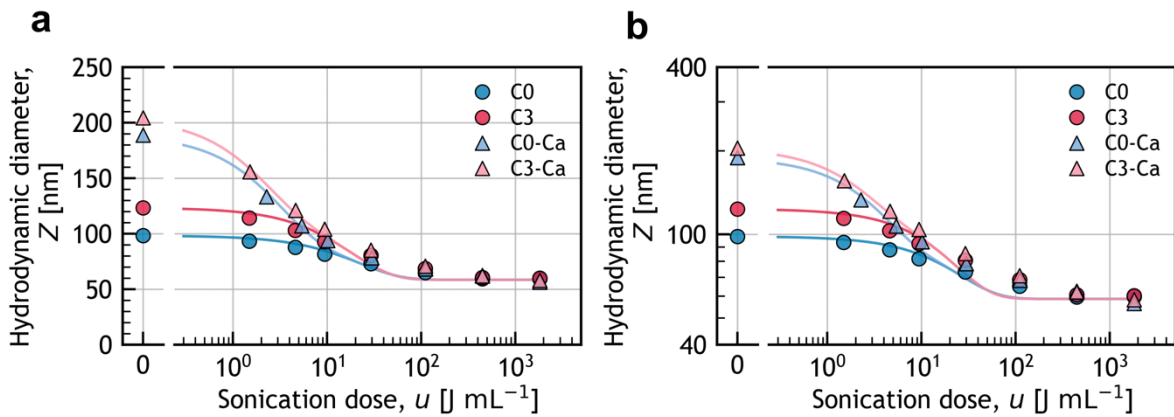


**Figure S10.** Evolution of the Z-average diameter ( $Z$ ) as a function of the sonication dose ( $u$ ) and best fit using **Equation S12** and **Equation S13**, with (a) a linear-log plot and (b) a log-log plot to highlight the bad fitting at intermediate sonication dose.

**Table S10.** Best fitting parameter ( $k$ ) and goodness of fit ( $R^2$  and MSE) for the evolution of the Z-average diameter as a function of the sonication dose using a simple dissociation function (**Equations S12** and **Equation S13**).

Sample	$k$ (mL J <sup>-1</sup> )	$R^2$	MSE
<b>C0</b>	$0.044 \pm 0.008$	0.95	9.9
<b>C3</b>	$0.054 \pm 0.010$	0.94	32.4
<b>C0-Ca</b>	$0.330 \pm 0.050$	0.98	32.6
<b>C3-Ca</b>	$0.460 \pm 0.100$	0.98	48.3

Interestingly,  $\ln(-dZ/du)$  exhibited an almost linear relationship with  $\ln(u Z)$  (see **Figure S11**). Therefore, the evolution of  $Z$  (nm) as a function of  $u$  (J mL<sup>-1</sup>) was modelled by a modified dissociation equation:

$$\frac{dZ}{du} = -k'(u) Z \quad (\text{S15})$$

with:

$$k'(u) = k^\alpha \alpha u^{\alpha-1} \quad (\text{S16})$$

where  $k'$  (mL J<sup>-1</sup>) is a dose-dependent factor of size decrease,  $k$  is a constant and  $\alpha$  is a stretching exponent. Integrating this expression leads to **Equation 5** and **Equation 6**, that were used to fit the data presented in **Figure 6**. The best fitting parameters are summarized in **Table S11**.

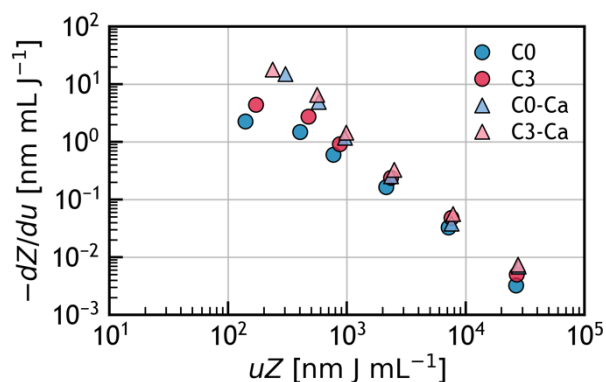


**Figure S11.** Evolution of  $-dZ/du$  as a function of the product of the sonication dose and the size ( $u Z$ ).

**Table S11.** Best fitting parameters ( $k$  or  $k_{Ca}$  and  $\alpha$  or  $\alpha_{Ca}$ ) and goodness of fit ( $R^2$  and MSE) for the evolution of the Z-average diameter as a function of the sonication dose using a modified dissociation function (Equation 5 and Equation 6).

Sample	$k$ or $k_{Ca}$ (mL J <sup>-1</sup> )	$\alpha$ or $\alpha_{Ca}$	$R^2$	MSE
C0	0.030 ± 0.003	0.57 ± 0.04	1.00	1.0
C3	0.036 ± 0.004	0.53 ± 0.04	0.99	3.5
C0-Ca	0.300 ± 0.030	0.66 ± 0.09	1.00	6.4
C3-Ca	0.340 ± 0.030	0.74 ± 0.09	1.00	5.2

## S7. Self-organization of CNCs

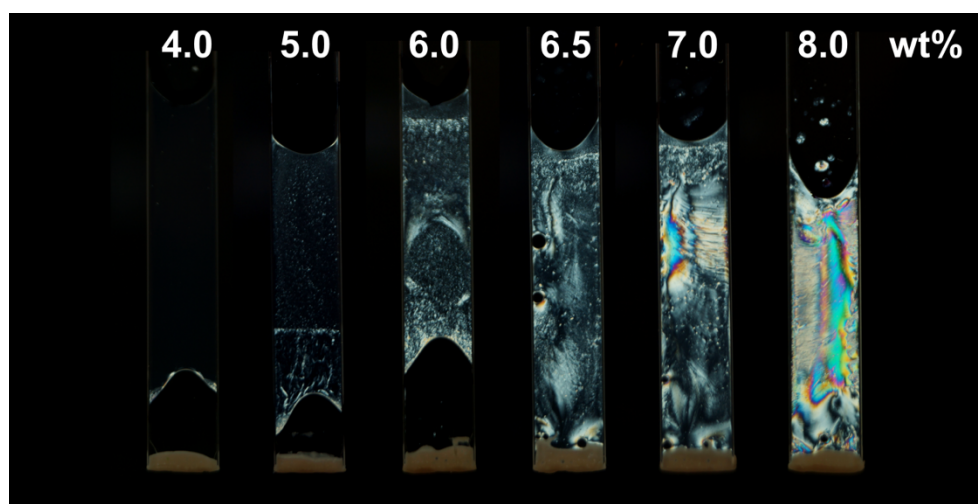


**Figure S12.** Photograph of a series of capillaries containing calcium-CNC suspension (Ca-C3) with increasing weight fraction.

### Studying the Impact of Salt Condition on the CNC Self-Organization

To illustrate the practical significance of our findings for CNC self-organization, we performed a series of experiments using sonicated CNCs (sonication doses 12, 192 and 768 J mL<sup>-1</sup>) from our previous study.<sup>[10]</sup> For each sample, a mother suspension of concentrated CNCs (> 10 wt%) was prepared in the presence of NaCl (1.2 mM wt%<sup>-1</sup>) before being diluted with ultrapure water to obtain a range of CNC volume fractions ( $\Phi$ ) at fixed ratio of NaCl per CNC. The self-assembly behavior of these suspensions was investigated and the Z-average diameter of the CNCs after dilution (0.1 wt%, 1 mM NaCl) was measured and compared to their value before concentration in the presence of salt.

The evolution of the anisotropic volume fraction ( $\phi_{ani}$ ) as a function of  $\Phi$  for each sample is presented in **Figure S13a**. The  $\phi_{ani}$  for all samples were superimposed, with an appearance of the anisotropic phase around 2 vol% followed by a sigmoid increase until a fully anisotropic

phase is reached around 7 vol%. The corresponding pitches ( $p$ ), presented in **Figure S13b**, exhibited a similar decrease with  $\Phi$  for all samples, whatever their sonication history. These results are in stark contrast with the behavior of the same suspensions without salt,<sup>[10]</sup> for which the self-assembly behavior was dependent of the sonication dose. Moreover, all samples that were concentrated in salt also exhibited an increase of Z-average diameter (**Figure S13c**).

Overall, this experiment shows that a suspension of CNCs reaching 12 mM of NaCl can lead to irreversible morphological changes that impact subsequent self-organization. While adding salt to a CNC suspension is known to shifts its biphasic regime to higher  $\Phi$  and its pitch to lower values,<sup>[61]</sup> to our knowledge, such superimposition of the self-organization values for different samples was never reported. These observations are coherent with the irreversible formation of bundles upon concentration of the CNCs in the presence of salt, leading to a shift of the biphasic regime toward lower  $\Phi$  and to lower pitches. However, further work is needed to elucidate the exact origin of the superimpositions of the  $\Phi$  and pitch values, despite the size differences between the samples.

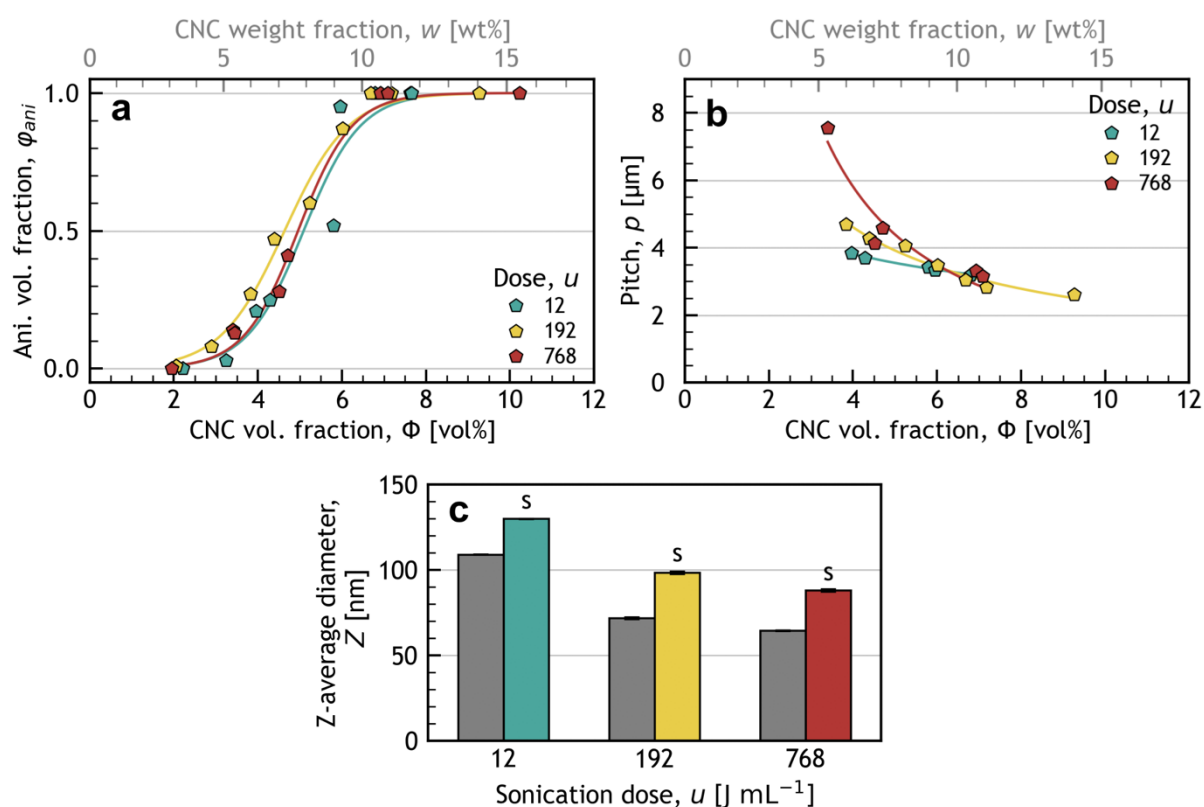


**Figure S13.** Evolution of the **(a)** anisotropic phase volume fraction ( $\phi_{ani}$ ) and **(b)** pitch ( $p$ ) as a function of the CNC volume fraction ( $\Phi$ ) for sonicated samples (12, 192 and 768 J mL<sup>-1</sup>) at fixed ratio of NaCl per CNC (1.2 mM wt%<sup>-1</sup>), after concentration in the presence of NaCl (> 10 wt% CNCs, > 12 mM NaCl). **(c)** Z-average diameter ( $Z$ ) of the CNCs (at 0.1 wt% in 1 mM NaCl) before (grey) and after (colored) concentration in salt.